Geol. Mag. **156** (*4*), *2019, pp. 683–701* © *Cambridge University Press 2018*
doi:10.1017/S0016756818000122

Detrital zircon geochronology and geochemistry of Jurassic sandstones in the Xiongcun district, southern Lhasa subterrane, Tibet, China: implications for provenance and tectonic setting

XINGHAI LANG*‡, DONG LIU§†, YULIN DENG*, JUXING TANG¶, XUHUI WANG*, ZONGYAO YANG||, ZHIWEI CUI*, YONGXIN FENG*, QING YIN*, FUWEI XIE¶, YONG HUANG# & JINSHU ZHANG**

*College of Earth Science and MLR Key Laboratory of Tectonic Controls on Mineralization and Hydrocarbon Accumulation, Chengdu University of Technology, Chengdu 610059, China
‡State Key Laboratory of Continental Tectonics and Dynamics, Institute of Geology, Chinese Academy of Geological Sciences, Beijing 100037, China
§College of Management Science, Chengdu University of Technology, Chengdu 610059, China
¶Institute of Mineral Resources, Chinese Academy of Geological Sciences, Beijing 100037, China
||Faculty of Geosciences and Environmental Engineering, Southwest Jiaotong University, Chengdu 611756, China
#Chengdu Center of China Geological Survey, Chengdu 610081, China
**College of Engineering, Tibet University, Lhasa 850012, China

(*Received* 30 May 2017; *accepted* 27 January 2018; *first published online* 18 April 2018)

Abstract – Jurassic sandstones in the Xiongcun porphyry copper–gold district, southern Lhasa subterrane, Tibet, China were analysed for petrography, major oxides and trace elements, as well as detrital zircon U–Pb and Hf isotopes, to infer their depositional age, provenance, intensity of source-rock palaeo-weathering and depositional tectonic setting. This new information provides important evidence to constrain the tectonic evolution of the southern Lhasa subterrane during the Late Triassic – Jurassic period. The sandstones are exposed in the lower and upper sections of the Xiongcun Formation. Their average modal abundance ($Q_{21}F_{11}L_{68}$) classifies them as lithic arenite, which is also supported by geochemical studies. The high chemical index of alteration values (77.19–85.36, mean 79.96) and chemical index of weathering values (86.19–95.59, mean 89.98) of the sandstones imply moderate to intensive weathering of the source rock. Discrimination diagrams based on modal abundance, geochemistry and certain elemental ratios indicate that felsic and intermediate igneous rocks constitute the source rocks, probably with a magmatic arc provenance. The detrital zircon ages (161–243 Ma) and $\varepsilon_{Hf}(t)$ values (+10.5 to +16.2) further constrain the sandstone provenance as subduction-related Triassic–Jurassic felsic and intermediate igneous rocks from the southern Lhasa subterrane. A tectonic discrimination method based on geochemical data of the sandstones, as well as detrital zircon ages from sandstones, reveals that the sandstones were most likely deposited in an oceanic island-arc setting. These results support the hypothesis that the tectonic background of the southern Lhasa subterrane was an oceanic island-arc setting, rather than a continental island-arc setting, during the Late Triassic – Jurassic period.

Keywords: Jurassic, sandstone, detrital zircons, geochemistry, Lhasa terrane

1. Introduction

Sandstones have been effectively used to constrain provenance and identify ancient tectonic settings (e.g. Bhatia, 1983; Dickinson *et al.* 1983; McLennan *et al.* 1993; Osae *et al.* 2006; Chen *et al.* 2016). Provenance and tectonic setting constraints of sandstones can be determined in a variety of ways, including petrographic analysis, chemical index of alteration, whole-rock chemistry, and zircon U–Pb and Lu–Hf isotopic analyses (Han *et al.* 2012; Chen *et al.* 2016). The petrographic features and chemical index of sandstones can be used to help interpret their sedimentary environment, source area and tectonic depositional setting (Dickinson & Suczek, 1979; Dickinson *et al.* 1983; Chen *et al.* 2016). The chemical composition of sandstones, such as major elements ($Fe_2O_3^* + MgO$), TiO_2, Al_2O_3/SiO_2 and K_2O/Na_2O, immobile elements such as La, Th, Sc and Zr, and their ratios, can further reveal their tectonic setting and provenance (Bhatia & Crook, 1986; McLennan & Taylor, 1991; McLennan *et al.* 1993; Griffin *et al.* 2004; Sun, Gui & Chen, 2012; Shi *et al.* 2016). The zircon Lu–Hf isotope compositions combined with U–Pb ages from zircons within sandstones can provide further valuable information on the provenance, depositional age and tectonic setting of sedimentary basins (Andersen, 2005; Augustsson *et al.* 2006; Cawood, Hawkesworth & Dhuime, 2012; Chen *et al.* 2016; Du *et al.* 2016).

The southern Lhasa subterrane (Fig. 1b) has formed as a result of the tectonic evolution from the subduction of the Neo-Tethys oceanic slab that was initiated during Late Triassic time or even earlier (Mo *et al.* 2005*b*; Chu *et al.* 2006, 2011; Zhang *et al.* 2007;

†Author for correspondence: liudong@cdut.edu.cn

https://doi.org/10.1017/S0016756818000122 Published online by Cambridge University Press

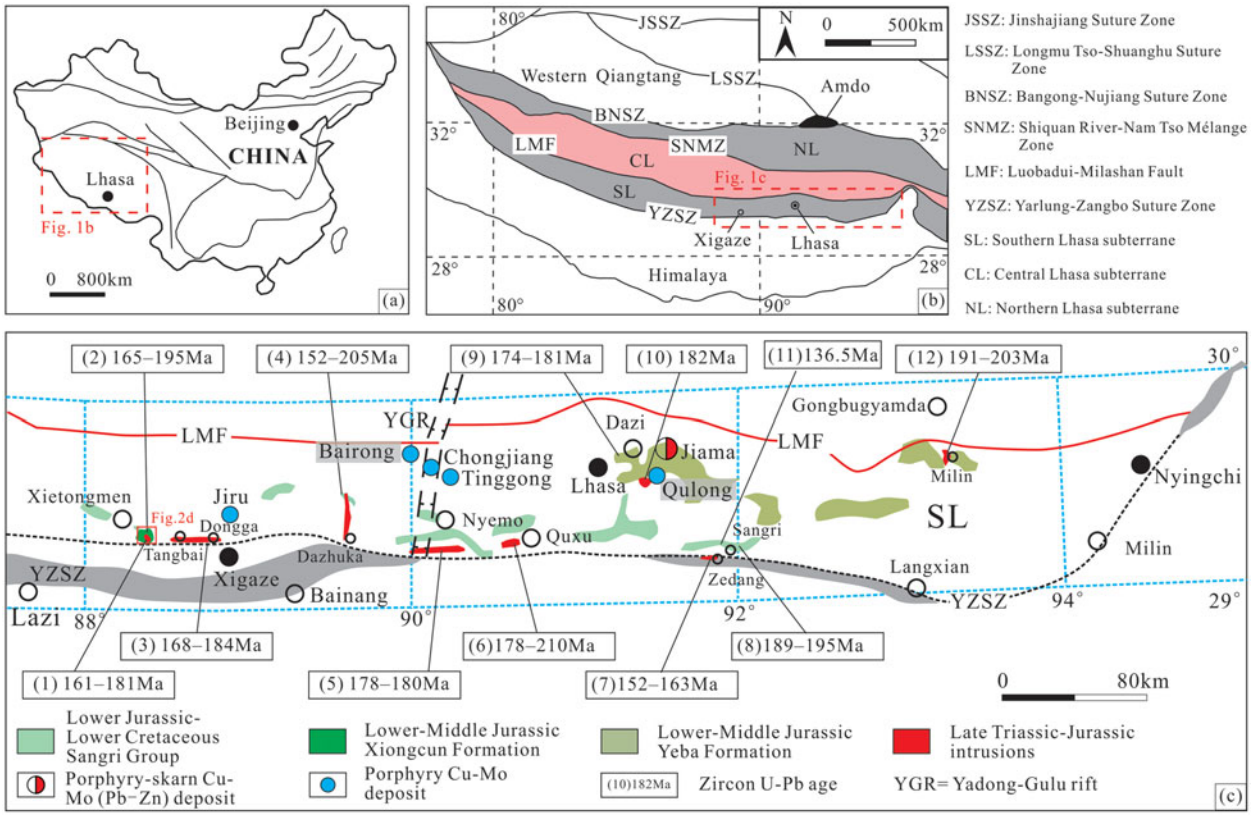

Figure 1. (Colour online) Simplified map of: (a) China, showing the location of the Himalayan–Tibetan orogeny; (b) regional geology of the Himalayan–Tibetan orogen, showing the location of the study region (modified from Zhu *et al.* 2011*b*); and (c) geology of the study region, showing the distribution of Triassic–Jurassic igneous rocks related to the subduction of the Neo-Tethys oceanic slab (modified from Zhu *et al.* 2008; Hou *et al.* 2015*b*). Data source: (1) Lang *et al.* (2014); (2) Qu *et al.* (2007*b*) and Tang *et al.* (2010); (3) Guo *et al.* (2013) and Qiu *et al.* (2015); (4) Chu *et al.* (2006), Ji *et al.* (2009), Guo *et al.* (2013) and Meng *et al.* (2016*a*); (5) Zhang *et al.* (2007) and Guo *et al.* (2013); (6) Meng *et al.* (2016*b*); (7) McDermid *et al.* (2002); (8) Kang *et al.* (2014); (9) Geng *et al.* (2006) and Zhu *et al.* (2008); (10) Yang *et al.* (2008); (11) Zhu *et al.* 2009; and (12) Zhu *et al.* (2011*b*).

Ji *et al.* 2009; Tang *et al.* 2010; Guo *et al.* 2013; Lang *et al.* 2014; Meng *et al.* 2016*b*), to the Indian–Asian continental collision which began during Paleocene time (*c.* 65–50 Ma) (Yin & Harrison, 2000; Mo *et al.* 2003; Ding, Kapp & Wan, 2005). Previous investigations of the southern Lhasa subterrane have focused on the initial timing of the India–Asia collision and the Cretaceous–Cenozoic magmatism and sedimentation (e.g. Yin & Harrison, 2000; Mo *et al.* 2008; Kapp *et al.* 2005, 2007*a*, *b*; Volkmer *et al.* 2007). By contrast, the Late Triassic – Jurassic tectonic evolution of the southern Lhasa subterrane is relatively poorly understood and even a controversial subject. Over the past few years, some studies have reported that the geological setting of the southern Lhasa subterrane was a continental island-arc setting during the Late Triassic–Jurassic period (e.g. Yang *et al.* 2008; Zhu *et al.* 2008; Ji *et al.* 2009; Guo *et al.* 2013; Meng *et al.* 2016*a*, *b*; Wang *et al.* 2016; Ma *et al.* 2017*a*), whereas others have suggested that it was probably an oceanic island-arc setting (Aitchison, Ali & Davis, 2007; Kang *et al.* 2014; Huang *et al.* 2015; Tang *et al.* 2015; Lang *et al.* 2017; Ma *et al.* 2017*b*; Ma, Yi & Xu, 2017; Yin *et al.* 2017). This controversy limits our understanding of the tectonic evolution of the southern Lhasa subterrane. Moreover, the Kohistan–Ladakh block, which is located to the west of Lhasa terrane, has been recognized as an oceanic island arc related to subduction of the Neo-Tethys oceanic slab (Rolland, Pêcher & Picard, 2000; Mahéo *et al.* 2004; Ahmad *et al.* 2008). The key issue is whether the tectonic setting of the southern Lhasa subterrane resembles the Kohistan–Ladakh block. To determine the early Mesozoic tectonic evolution of the southern Lhasa subterrane, most researchers have focused on the geochemistry and geochronology of the Upper Triassic – Jurassic igneous rocks distributed in the southern Lhasa subterrane; however, contemporaneous sedimentary rocks were not considered. Sedimentary rocks can provide effective information with which to constrain the ancient tectonic setting, and it is also a far more reliable guide to tectonic setting than the compositions of the volcanic rocks themselves (Li *et al.* 2015). We therefore present in this paper the petrology, geochemical composition, detrital zircon U–Pb age and Lu–Hf isotopes of sandstones from the Lower–Middle Jurassic Xiongcun Formation within the southern Lhasa subterrane to constrain their depositional age and to deduce provenance and tectonic setting. The results provide additional information for reconstructing the tectonic evolution of the southern Lhasa subterrane during the Late Triassic – Jurassic period.

https://doi.org/10.1017/S0016756818000122 Published online by Cambridge University Press

2. Geological background and sampling

2.a. Geological background

The Lhasa terrane is bound to the north by the Banggong–Nujiang Suture Zone (BNSZ) and to the south by the Yarlung–Zangbo Suture Zone (YZSZ; Fig. 1b; Yin & Harrison, 2000). It can be divided into northern, central and southern subterranes by the Shiquan River–Nam Tso Mélange Zone (SNMZ) and the Luobadui–Milashan Fault (LMF; Fig. 1b; Zhu *et al.* 2011*b*). This study is mainly focused on the southern Lhasa subterrane (Fig. 1b, c), characterized by juvenile crust (Hou *et al.* 2015*b*). In the southern Lhasa subterrane, the sedimentary cover is limited and is mainly of the Lower Jurassic – Tertiary volcanic-sedimentary sequences (Mo *et al.* 2005*b*; Pan *et al.* 2006; Tang *et al.* 2007; Zhu *et al.* 2009, 2011*b*; Kang *et al.* 2014). The Jurassic–Cretaceous volcanic-sedimentary sequences primarily includes the Lower–Middle Jurassic Yeba and Xiongcun formations as well as the Lower Jurassic – Lower Cretaceous Sangri Group (Fig. 1c; Pan *et al.* 2006; Zhu *et al.* 2008, 2009; Kang *et al.* 2014). The Tertiary volcanic-sedimentary sequence is predominantly the Paleocene–Eocene Linzizong volcanic succession, which consists of the andesitic lower Dianzhong Formation, dacitic middle Nianbo Formation and rhyolitic upper Pana Formation (Mo *et al.* 2003; Lee *et al.* 2009).

Magmatic activity in the southern Lhasa subterrane was related to the northwards subduction of the Neo-Tethys oceanic slab and the subsequent collision of the Indian and Eurasian plates (Yin & Harrison, 2000; Mo *et al.* 2005*a*; Ji *et al.* 2009; Chu *et al.* 2011; Li *et al.* 2011; Lang *et al.* 2014). The Late Triassic–Jurassic and Cretaceous arc volcanic rocks, granitoid intrusions, and porphyries in the southern Lhasa subterrane were formed in a subduction geologic setting (Fig. 1c; Chu *et al.* 2006; Qu *et al.* 2007*b*; Zhang *et al.* 2007; Yang *et al.* 2008; Wen *et al.* 2008; Ji *et al.* 2009; Tang *et al.* 2010; Guo *et al.* 2013; Lang *et al.* 2014). The Paleocene–Eocene Linzizong volcanism, voluminous granitoid batholiths and porphyries formed in a continental collisional geological setting (Mo *et al.* 2005*b*, 2008; Chu *et al.* 2006; Ji *et al.* 2009; Lee *et al.* 2009). The Miocene intrusions, which formed in a post-collisional geological setting and have an adakite-like affinity, were commonly emplaced as small stocks and/or dykes in the southern Lhasa subterrane (Hou *et al.* 2004; Chung *et al.* 2005; Qu *et al.* 2007*a*; Wang *et al.* 2014*a*, *b*).

The strata exposed in the Xiongcun district belong to the Lower–Middle Jurassic Xiongcun Formation, which are mainly exposed near the Xiongcun village, Xietongmen County, southern Lhasa subterrane (Fig. 1). The Xiongcun Formation is divided into three volcanic-sedimentary successions. From bottom to top, these include: (1) a lower section composed of volcanic breccia as well as minor lava, tuff, sandstone and siltstone interlayered with argillite; (2) a middle section composed of tuff and minor lava and siltstone interlayered with argillite; and (3) an upper section composed of sandstone and siltstone interlayered with argillite as well as minor tuff, conglomerate and limestone (Tang *et al.* 2007). The intrusive rocks in the Xiongcun district are of Jurassic and Eocene age (Fig. 2a; Lang *et al.* 2017). The Jurassic intrusions include Early Jurassic quartz diorite porphyry, Early–Middle Jurassic quartz diorite porphyry, Middle Jurassic quartz diorite porphyry and diabase dykes, and Late Jurassic gabbro. The Eocene intrusions include biotite granodiorite, quartz diorite, granitic aplite dykes and lamprophyre dykes. Three porphyry copper–gold deposits (No. 1, No. 2 and No. 3) have been discovered in the Xiongcun district (Fig. 2a). The mineralization was hosted in the Jurassic porphyries and the surrounding contemporary volcanic rocks (Tafti *et al.* 2009, 2014; Lang *et al.* 2014, 2017; Tang *et al.* 2015). The No. 1 deposit is associated with the Middle Jurassic quartz diorite porphyry and formed at *c.* 161.5 ± 2.7 Ma (Lang *et al.* 2014); the No. 2 deposit is associated with the Early Jurassic quartz diorite porphyry and formed at 174.4 ± 1.6 Ma (Lang *et al.* 2014); and the No. 3 deposit is a newly discovered deposit.

2.b. Sampling

Sandstone samples for this study were collected from outcrops of the Xiongcun Formation in the Xiongcun district. Eight of the least weathered samples from the lower section (two samples, BL21-06-04 and BL21-06-05) and upper section (six samples, BL01-14-1, BL01-14-3, BL01-14-4, BL12-07-1, BL12-07-2 and BL12-08-2) of the Xiongcun Formation were studied. The location of samples is shown in the geological map (Fig. 2a) along with a typical cross-section (Fig. 2b) and a stratigraphic column (Fig. 3). The exact locations of the studied samples are given in Table 1.

3. Methodology

3.a. Petrographic analysis

To observe sample petrographic textures, photomicrographs were taken using a Nikon polarized microscope at the Key Laboratory of Tectonic Controls on Mineralization and Hydrocarbon Accumulation, Chengdu University of Technology. Point counting in thin-sections of the sandstones was used to quantify the mineral abundances. Modal analysis was performed by the Gazzi–Dickinson counting method (Gazzi, 1966; Dickinson, 1970). Zircon cathodoluminescence (CL) images were taken using a FEI Quanta 200F scanning electron microscope at Nanjing Hongchuang Dikan Co., Ltd.

3.b. Whole-rock geochemical analysis

The whole-rock major- and trace-element concentrations of eight sandstone samples (BL01-14-1,

https://doi.org/10.1017/S0016756818000122 Published online by Cambridge University Press

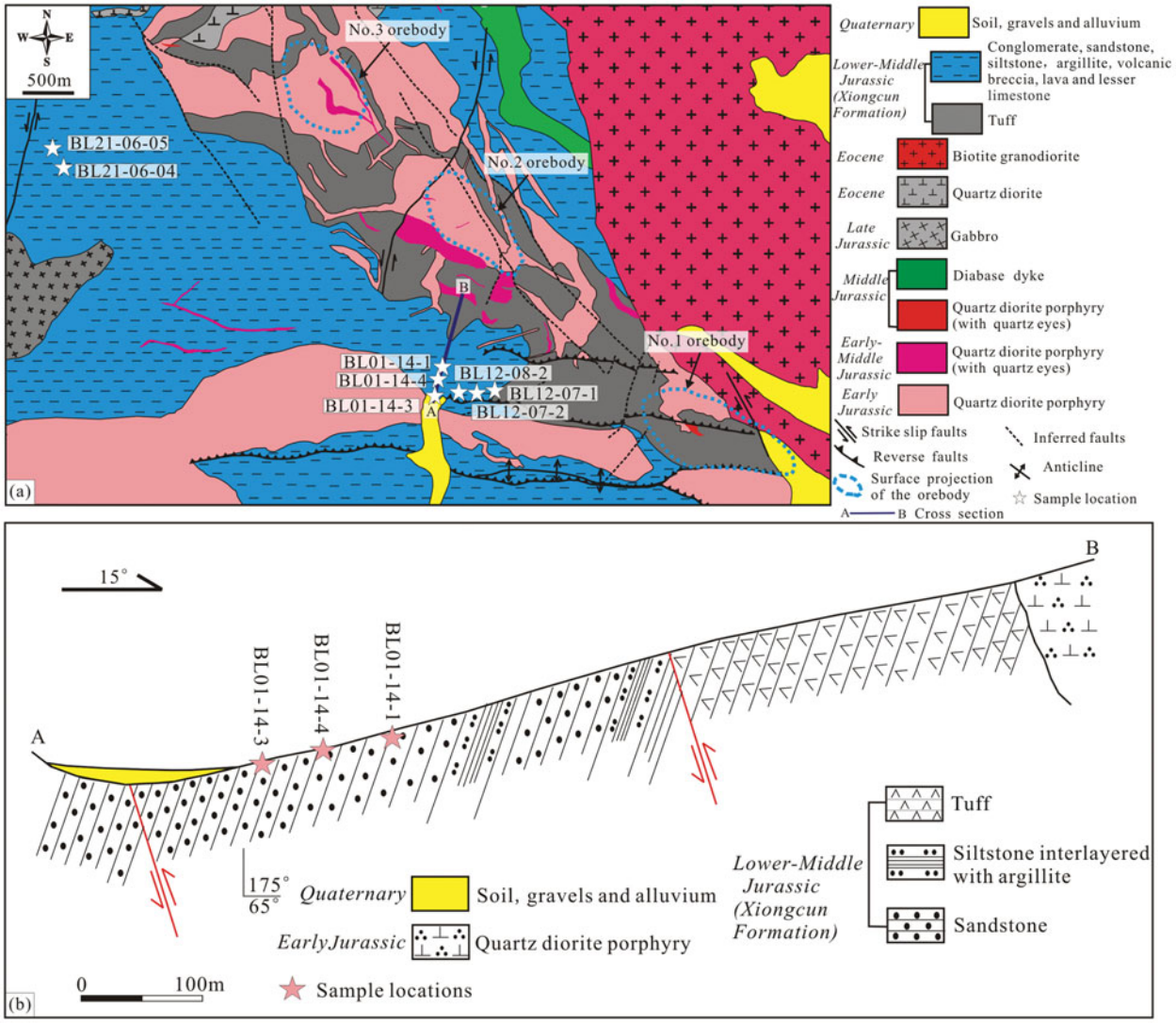

Figure 2. (Colour online) (a) Geological map of the Xiongcun district, showing the sampling locations (modified from Lang *et al.* 2012); and (b) A–B cross-section in the Xiongcun district, showing the sampling locations (BL01-14-1, BL01-14-3 and BL01-14-4). The location of the A–B cross-section is shown in Figure 2a.

Table 1. Framework modal analytical results of the lithic sandstones in the Xiongcun Formation.

Samples	Location	Qm	Qp	Pl	KF	Lv	Lm	Ls	Total	Q (%)	F (%)	L (%)
BL01-14-1	88° 24′ 11.8″ N, 29° 22′ 4.8″ E	81	10	17	12	179	9	18	326	28	9	63
BL01-14-3	88° 24′ 11.3″ N, 29° 22′ 0.4″ E	69	8	23	18	218	13	15	364	21	11	68
BL01-14-4	88° 24′ 11.4″ N, 29° 22′ 2.7″ E	46	11	14	23	196	8	13	311	18	12	70
BL12-07-1	88° 24′ 18.3″ N, 29° 22′ 0.7″ E	61	15	18	10	203	11	16	334	23	8	69
BL12-07-2	88° 24′ 18.5″ N, 29° 22′ 1.7″ E	50	14	26	14	200	11	12	327	20	12	68
BL12-08-2	88° 24′ 19.1″ N, 29° 22′ 2.6″ E	59	9	16	13	212	7	8	324	21	9	70
BL21-06-04	88° 21′ 53.5″ N, 29° 23′ 18.3″ E	43	7	16	12	167	9	7	261	19	11	70
BL21-06-05	88° 21′ 50.3″ N, 29° 23′ 20.8″ E	54	3	20	9	171	24	7	288	20	10	70

Qm – monocrystalline quartz; Qp – polycrystalline quartz; Pl – plagioclase; KF – K-feldspar; Lm – metamorphic rock fragment; Lv – volcanic rock fragment; Ls – sedimentary rock fragment; Q = Qm + Qp, total number of quartz grains; F = Pl + KF, feldspar; L = Lv + Lm + Ls, lithic grains

BL01-14-3, BL01-14-4, BL12-07-1, BL12-07-2, BL21-08-2, BL21-06-04 and BL21-06-05) were determined at the analytical laboratory of the Beijing Research Institute of Uranium Geology. Whole-rock major elements were analysed using X-ray fluorescence (XRF). Powder samples of approximately 0.5 g were mixed with 5 g $Li_2B_4O_7$ to make glass disks, which were then analysed using an AXIOS mineral spectrometer. The accuracy of XRF analysis was within 5 %. Whole-rock trace elements, including rare Earth elements (REEs), were analysed using a Finnigan Element inductively coupled plasma mass spectrometer (ICP-MS) after acid digestion of the samples in high-pressure Teflon bombs. The detailed analytical procedures are described in Qi, Hu & Grégoire (2000) and the analytical precision was

https://doi.org/10.1017/S0016756818000122 Published online by Cambridge University Press

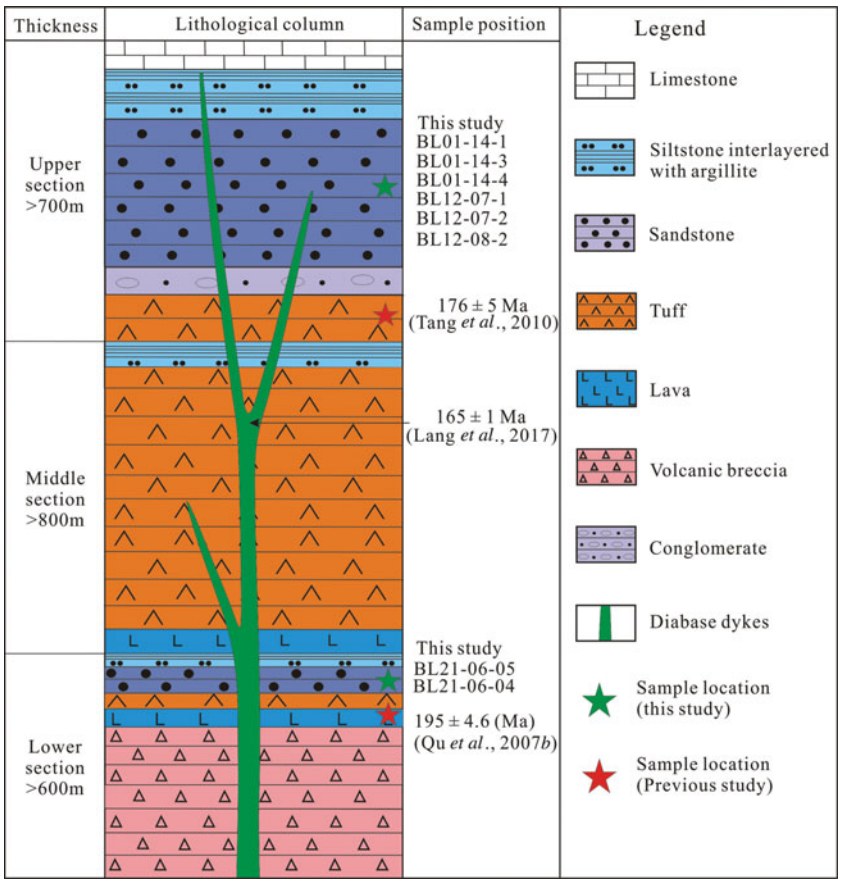

Figure 3. (Colour online) Stratigraphic column of the Xiongcun Formation in the Xiongcun district.

generally less than 5 % error. The chemical index of alteration (CIA) was calculated using the formula CIA $= 100 \times Al_2O_3/(Al_2O_3 + CaO^* + Na_2O + K_2O)$ (Nesbitt & Young, 1982). The chemical index of weathering (CIW) was calculated using the formula CIW $= 100 \times Al_2O_3/(Al_2O_3 + CaO^* + Na_2O)$ (Harnois, 1988). In the above equations, CaO^* is the content of CaO incorporated in the silicate fraction, and all major oxides are expressed in molar proportions. There is no direct method to distinguish and quantify the contents of CaO belonging to the silicate and non-silicate fractions (carbonates and apatite). Here we used the method reported by McLennan (1993) to calculate CaO^* ($CaO - 10/(3 \times P_2O_5)$). Function 1 (F1) and Function 2 (F2) were calculated via: $F1 = 0.074SiO_2 - (0.226Fe_2O_3) - (0.270Al_2O_3) + 4.489TiO_2 + 0.153CaO - (0.137MgO) + 0.398Na_2O + 1.447K_2O + 52.458P_2O_5 - (9.655)$; and $F2 = 0.190SiO_2 + 0.268Fe_2O_3 + 0.313Al_2O_3 - (0.336TiO_2) + 0.209CaO + 4.107MgO + 3.866Na_2O - (1.293K_2O) - (6.570P_2O_5) - 18.926$ (Tobia & Aswad, 2014).

3.c. Zircon LA-ICP-MS U–Pb dating method

Two sandstone samples (BL01-14-3 and BL21-06-05) were chosen for zircon U–Pb isotopic analyses. The analyses were performed using LA-ICP-MS at the State Key Laboratory of Continental Dynamics, Northwest University, Xi'an, China. Zircons were separated by heavy-liquid and magnetic separation methods. Pure zircons were handpicked under a binocular microscope, before being mounted in epoxy resin and polished until the grain interiors were exposed. Before analysis, the surface was cleaned using 3 % HNO_3 to remove any Pb contaminants. The sites for zircon U–Pb age analysis were selected on the basis of the CL imaging. During the analyses, a laser repetition rate of 6–8 Hz at 100 mJ was used, and the spot sizes were 40–60 μm. Every fifth sample analysis was followed by the analysis of a suite of zircon standards: Harvard zircon 91500 (Wiedenbeck *et al.* 1995), Australian National University standard zircon TEMORA 1 (Black *et al.* 2003) and NISTSRM 610. Each spot analysis consisted of approximately 30 s of background acquisition and 40 s of sample data acquisition. The $^{207}Pb/^{206}Pb$, $^{206}Pb/^{238}U$, $^{207}Pb/^{235}U$ ($^{235}U = {}^{238}U/137.88$) and $^{208}Pb/^{232}Th$ ratios were corrected using Harvard zircon 91500 (Wiedenbeck *et al.* 1995) as the external standard. Common Pb contents were evaluated using the method described by Andersen (2002). The isotopic ratios and element concentrations of the zircons were calculated using GLITTER (version 4.4.2, Macquarie University).

3.d. *In situ* zircon Hf analysis

In situ zircon Hf isotopic analysis was carried out at the Tianjin Center of China Geological Survey

https://doi.org/10.1017/S0016756818000122 Published online by Cambridge University Press

on relatively large zircon grains from the two sandstone samples (BL01-14-3 and BL21-06-05) that were also analysed for U–Pb isotopes. The Hf isotopes of those zircons were obtained using a Nu Plasma multi-collector MC-ICP-MS instrument coupled with a 193 nm ArF excimer laser-ablation system. The analytical method used is described by Tang *et al.* (2008) and He *et al.* (2013). The standard zircons Mud Tank and TEMORA were used in this analysis. A laser repetition rate of 8 Hz at 20 J cm^{-2} and a spot size of 44 μm were used. The isobaric interference of ^{176}Lu on ^{176}Hf was corrected by measuring the intensity of the interference-free ^{175}Lu isotope and using a recommended $^{176}Lu/^{175}Lu$ ratio of 0.02669 (De Bievre & Taylor, 1993) to calculate $^{176}Lu/^{177}Hf$. The $^{176}Yb/^{172}Yb$ value of 0.5886 (Chu *et al.* 2002) and the mean βYb value obtained during Hf analysis of the same spot were applied to correct for the interference of ^{176}Yb on ^{176}Hf (Iizuka & Hirata, 2005). The initial $^{176}Hf/^{177}Hf$ ratios were calculated with reference to the chondritic reservoir at the time of zircon growth from the magma. The decay constant of ^{176}Lu was 1.867×10^{-11} a^{-1} (Söerlund *et al.* 2004) in all calculations. For the calculation of $\varepsilon_{Hf}(t)$ values, we used chondritic ratios of $^{176}Hf/^{177}Hf = 0.282785$ and $^{176}Lu/^{177}Hf = 0.0336$ (Bouvier, Vervoort & Patchett, 2008). Single-stage model ages (T_{DM1}) were calculated using the measured $^{176}Lu/^{177}Hf$ ratios with reference to a model depleted mantle with a present-day $^{176}Hf/^{177}Hf$ ratio of 0.28325 and $^{176}Lu/^{177}Hf$ of 0.0384 (Griffin *et al.* 2002). Two-stage model ages (T_{DM2}) were calculated for the source rock of the magma by assuming a mean $^{176}Lu/^{177}Hf$ value of 0.015 for the average continental crust (Griffin *et al.* 2002).

4. Results

4.a. Petrography

The analysed sandstone samples from the Xiongcun Formation show yellow–grey colours, medium- to coarse-grain sizes, and angular to sub-angular shapes (Fig. 4). They are texturally immature, with very low degrees of rounding and sorting. The framework grains of the sandstones are mainly composed of lithic fragments (63–70 %, mostly volcanic rock fragments), quartz (18–28 %, monocrystalline and polycrystalline), feldspar (8–12 %, alkali feldspar and plagioclase), and minor detrital grains (<5 %) of muscovite, biotite, apatite and zircon (Fig. 4e, f; Table 1). The rocks have a high amount of matrix (15–20 %) composed of quartz, feldspar, muscovite and clay. According to their mineral constituents these sandstones can be classified as lithic arenite in a QFL diagram (Fig. 5a), indicating a magmatic-arc provenance (Fig. 5b). On the other hand, using the geochemical classification diagram of Taylor & McLennan (1985), the sandstones from the Xiongcun Formation are classified as graywackes and show magmatic-arc provenance (Fig. 5c).

4.b. Whole-rock geochemistry

The whole-rock major- and trace-element concentrations of Jurassic sandstones in the Xiongcun district are listed in Table 2.

4.b.1. Major elements

As shown in Table 2, it is apparent that the sandstone samples show moderate SiO_2 contents (53.27–66.13 %, mean 58.27 %) and high Al_2O_3 (14.53–24.04 %, mean 20.12 %) and FeO (3.25–10.65 %, mean 7.12 %) abundance. Meanwhile, these sandstones have low Na_2O (0.41–1.49 %, mean 0.85), TiO_2 (0.68–1.25 %, mean 0.91), CaO (0.54–1.87 %, mean 0.92), K_2O (1.04–3.75 %, mean 2.17), Fe_2O_3 (0.87–4.96 %, mean 2.39) and MgO (1.28–3.34 %, mean 2.35) abundance, with a collective total of less than 10 %. In addition, these sandstone samples show high $Fe_2O_3{}^* + MgO$ contents (7.26–17.60 %, mean 12.66 %) and Al_2O_3/SiO_2 ratios (0.22–0.45 %, mean 0.29 %). The calculated CIA and CIW values range over 77.19–85.36 (mean 79.96) and 86.19–95.59 (mean 89.98), respectively (Table 2). The F1 and F2 values range from –2.90 to 9.46 (mean 4.30) and 2.23 to 11.7 (mean 8.07), respectively (Table 2).

4.b.2. Trace elements

The Jurassic sandstones in the Xiongcun district exhibit similar REE compositions, with total REE contents ranging over 59.02–102.10 ppm (Table 2). The chondrite-normalized REE patterns (Fig. 6a; Sun & McDonough, 1989) of these sandstones exhibit moderate light REE (LREE) enrichment compared with heavy REE (HREE, $La_N/Yb_N = 4.33–8.54$), and generally present smooth patterns with slightly negative Eu anomalies (δEu = 0.63–1.10) (Table 2; Fig. 6a). The post-Archean average Australian shale (PAAS) -normalized REE patterns are widely used in the study of sedimentary rocks (Bhatia, 1985; Khan, Dar & Khan, 2012; Kurian *et al.* 2013). In the PAAS-normalized REE patterns (Fig. 6b; Taylor & McLennan, 1985), these sandstone samples show moderate LREE depletion when compared with HREE ($La_N/Yb_N = 0.45–0.88$), with moderately positive Eu anomalies (δEu = 0.99–1.70) and slightly negative Ce anomalies (δCe = 0.74–0.96) (Table 2; Fig. 6b). In addition, the sandstones show low abundances of La (12.2–20.9 ppm), Th (2.14–2.82 ppm), Hf (3.28–4.07 ppm) and Nb (3.60–8.50 ppm), and low ratios of Th/U (1.61–3.61) and La/Sc (0.42–1.05) (Table 2). They also show high abundances of Co (8.11–26.4 ppm) and Zr (98–131 ppm), and high ratios of La/Th (4.60–8.29), Zr/Th (40.0–54.7) and Co/Th (3.1–11.4) (Table 2).

4.c. LA-ICP-MS U–Pb ages

The detrital zircon crystals of sandstone samples BL01-14-3 and BL21-06-05 have similar features. They are mainly euhedral to subhedral with sizes

https://doi.org/10.1017/S0016756818000122 Published online by Cambridge University Press

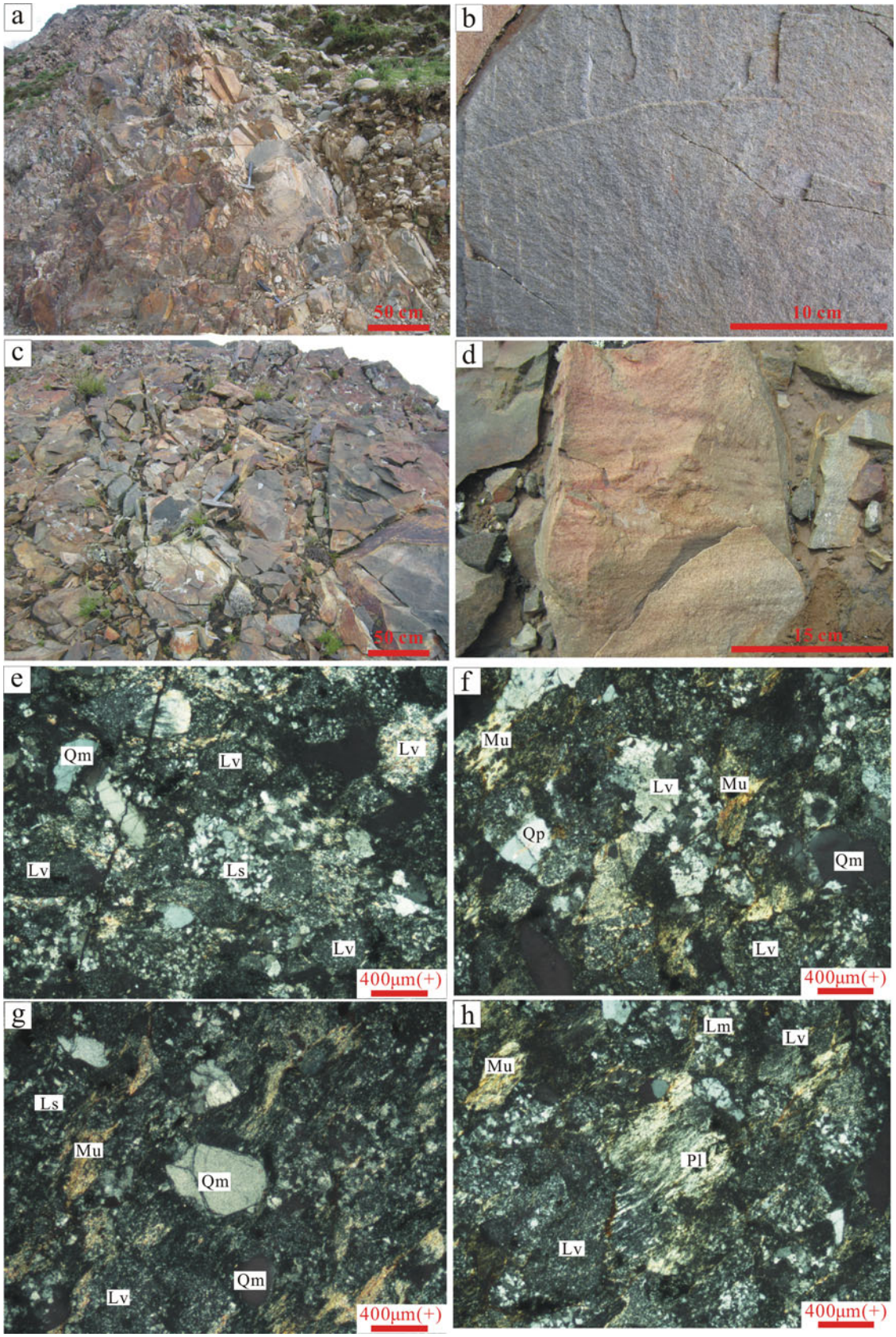

Figure 4. (Colour online) (a–d) Outcrop photos and (e–h) microphotos of the sandstones in the Xiongcun Formation. Qm – monocrystalline quartz; Qp – polycrystalline quartz; Pl – plagioclase; Lv – volcanic rock fragment; Ls – sedimentary rock fragment; Mu – muscovite.

https://doi.org/10.1017/S0016756818000122 Published online by Cambridge University Press

Table 2. Major oxides (%) and trace elements (ppm) of the sandstones in the Xiongcun Formation.

Sample	BL01-14-1	BL01-14-3	BL01-14-4	BL12-07-1	BL12-07-2	BL12-08-2	BL21-06-04	BL21-06-05	Average
SiO_2	63.02	63.13	66.13	57.43	53.38	56.29	53.54	53.27	58.27
TiO_2	0.71	0.79	0.68	0.95	0.99	0.74	1.25	1.15	0.91
Al_2O_3	15.64	19.56	14.53	23.50	24.04	18.29	23.13	22.30	20.12
Fe_2O_3	1.88	2.12	1.32	4.61	4.96	2.45	0.78	1.00	2.39
FeO	7.51	3.25	6.53	3.37	5.67	10.63	9.38	10.65	7.12
MnO	0.15	0.10	0.13	0.050	0.081	0.18	0.089	0.11	0.11
MgO	3.18	1.53	2.87	1.28	2.12	3.34	2.14	2.36	2.35
CaO	0.84	0.69	1.87	0.96	1.00	0.54	0.76	0.69	0.92
Na_2O	0.42	0.52	0.81	1.49	1.28	0.41	1.00	0.84	0.85
K_2O	2.03	3.75	1.44	1.54	1.04	1.76	3.01	2.79	2.17
P_2O_5	0.25	0.13	0.17	0.089	0.078	0.18	0.18	0.18	0.16
LOI	3.81	3.85	3.02	4.61	5.16	4.65	4.10	4.19	4.17
Total	99.44	99.43	99.51	99.88	99.80	99.46	99.35	99.54	99.55
$Fe_2O_3^*$+MgO	13.41	7.26	11.45	9.64	13.38	17.60	13.34	15.20	12.66
Al_2O_3/SiO_2	0.25	0.31	0.22	0.41	0.45	0.32	0.43	0.42	0.35
$Al_2O_3/(CaO+Na_2O)$	12.41	16.17	5.42	9.59	10.54	19.25	13.14	14.58	11.40
CIA	81.35	77.19	77.46	80.60	83.16	85.36	79.77	80.99	79.96
CIW	93.72	93.80	86.19	87.21	88.27	95.59	91.70	92.81	89.98
F1	9.46	5.15	5.29	−1.07	−2.90	4.12	7.52	6.80	4.30
F2	8.80	2.23	10.6	8.90	11.7	9.86	6.01	6.35	8.07
La	20.9	15.4	16.8	15.2	20.0	12.5	17.6	12.2	16.3
Ce	35.4	23.4	32.1	28.8	31.1	25.9	29.5	17.5	28.0
Pr	4.66	2.86	3.74	3.44	4.12	3.10	4.04	2.44	3.55
Nd	22.2	13.4	18.5	16.6	20.0	15.3	20.3	12.3	17.3
Sm	4.15	2.60	4.05	3.61	4.20	3.30	4.64	3.12	3.71
Eu	1.11	0.84	1.47	1.21	1.30	0.84	0.91	0.77	1.06
Gd	4.04	2.42	3.99	3.31	3.53	3.09	3.98	3.04	3.43
Tb	0.61	0.36	0.59	0.46	0.49	0.44	0.57	0.46	0.50
Dy	3.38	1.99	3.25	2.44	2.49	2.52	3.06	2.6	2.72
Ho	0.71	0.43	0.66	0.51	0.50	0.50	0.61	0.54	0.56
Er	2.09	1.32	1.86	1.52	1.45	1.46	1.73	1.56	1.62
Tm	0.32	0.21	0.27	0.23	0.21	0.21	0.26	0.23	0.24
Yb	2.19	1.48	2.09	1.72	1.68	1.77	2.53	2.02	1.94
Y	18.89	14.7	18.8	15.67	17.49	15.08	21.15	19.35	17.64
Lu	0.34	0.24	0.27	0.25	0.23	0.23	0.27	0.24	0.26
Li	49.7	28.7	41.6	28.6	31.3	60.1	46.6	59	43.2
Be	1.06	1.44	0.90	2.07	2.19	1.17	2.11	1.98	1.62
Sc	20.0	18.7	19.2	27.8	25.3	18.7	31.1	28.9	23.7
V	135	153	135	228	222	179	320	303	209
Cr	24.9	28.3	25.5	46.2	48.9	32.1	60.7	58.3	40.6
Co	14.5	14.9	15.7	8.11	11.3	12.2	24.3	26.4	15.9
Ni	12.9	14.1	13.2	9.65	15	15	21.9	28.7	16.3
Cu	23.7	38.7	22.2	136	95.8	221	39.4	46.5	77.9
Zn	155	150	114	51.7	88.8	138	429	189	164
Ga	18.2	20.5	16.2	23.8	27.2	21.4	25.2	30.1	22.8
Rb	49.9	78.5	39.9	43.1	33.3	56.4	79.1	85.1	58.2
Sr	104	162	154	293	274	109	307	256	207
Zr	111	131	107	119	121	98	117	106	114
Nb	4.16	5.53	3.60	4.88	5.77	4.10	8.50	5.66	5.28
Mo	1.04	1.41	0.28	0.95	1.18	0.4	0.89	1.97	1.02
Cs	3.37	3.62	3.52	5.53	5.61	2.62	3.48	3.8	3.94
Ba	341	566	230	244	355	197	683	739	419
Hf	3.41	4.07	3.28	3.45	3.81	3.41	3.66	3.83	3.62
Ta	0.43	0.4	0.28	0.37	0.87	0.56	1.24	0.41	0.57
W	0.86	0.99	1.02	0.72	0.72	0.87	2.88	0.59	1.08
Pb	123	60.6	64.4	96.1	1130	458	139	478	319
Bi	0.18	0.26	0.12	0.14	0.15	0.08	0.08	0.32	0.17
Th	2.52	2.82	2.23	2.62	2.63	2.38	2.14	2.65	2.50
U	0.73	1.04	0.64	0.84	0.94	0.66	0.88	1.65	0.92
Th/U	3.45	2.71	3.48	3.12	2.80	3.61	2.43	1.61	2.90
La/Sc	1.05	0.82	0.88	0.55	0.79	0.67	0.57	0.42	0.72
La/Th	8.29	5.46	7.53	5.80	7.60	5.25	8.22	4.60	6.60
Zr/Th	44.0	46.5	48.0	45.4	46.0	41.2	54.7	40.0	45.7
Co/Th	5.75	5.28	7.04	3.10	4.30	5.13	11.4	9.96	6.37
ΣREE	102.10	66.95	89.64	79.30	91.30	71.16	90.00	59.02	81.18
LREE	88.42	58.50	76.66	68.86	80.72	60.94	76.99	48.33	69.93
HREE	13.68	8.45	12.98	10.44	10.58	10.22	13.01	10.69	11.26
LREE/HREE	6.46	6.92	5.91	6.60	7.63	5.96	5.92	4.52	6.21
La_N/Yb_N[a]	6.85	7.46	5.77	6.34	8.54	5.07	4.99	4.33	6.05
δEu[a]	0.82	1.01	1.10	1.05	1.00	0.79	0.63	0.75	0.89
δCe[a]	0.84	0.80	0.95	0.94	0.80	0.99	0.83	0.74	0.86
La_N/Yb_N[b]	0.70	0.77	0.59	0.65	0.88	0.52	0.51	0.45	0.62
δEu[b]	1.26	1.56	1.70	1.63	1.57	1.23	0.99	1.16	1.38
δCe[b]	0.82	0.81	0.93	0.92	0.79	0.96	0.80	0.74	0.84

Normalized data after [a]Sun & McDonough (1989) and [b]Taylor & McLennan (1985)

https://doi.org/10.1017/S0016756818000122 Published online by Cambridge University Press

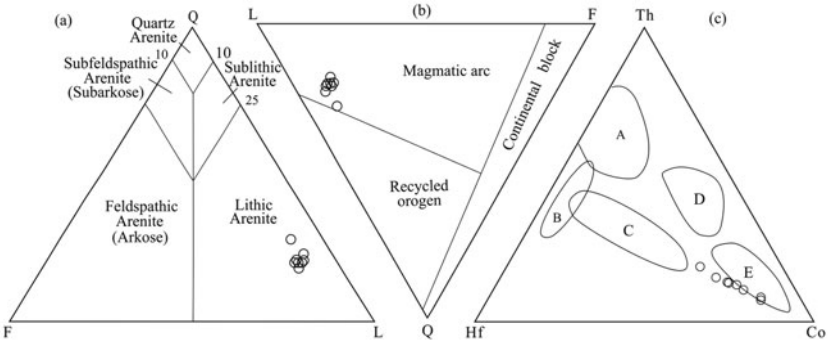

Figure 5. (a) QFL classification diagram (after Okada, 1971), (b) QFL provenance diagram (after Dickinson, 1985) and (c) Th–Hf–Co discrimination diagram (after Taylor & McLennan, 1985) for the sandstones in the Xiongcun Formation. A – felsic volcanic rocks; B – quartzite from cratonic basin; C – feldspar sandstones; D – shale (average upper continental crust); E – greywackes (arcs).

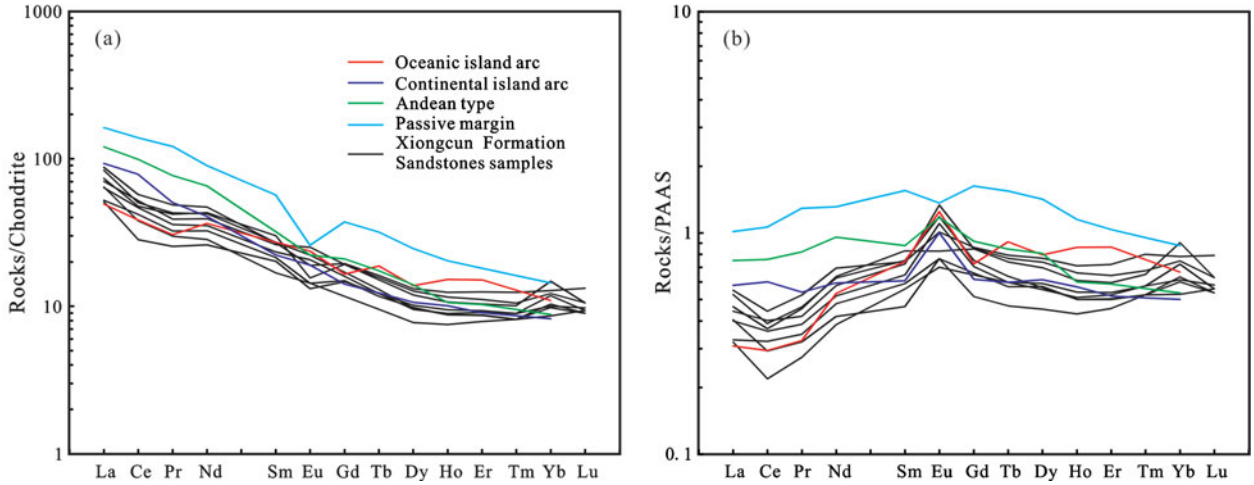

Figure 6. (Colour online) (a) Chondrite (after Sun & McDonough, 1989) and (b) post-Archean average Australian shale (PAAS) (after Taylor & McLennan, 1985) -normalized REE discriminatory plots for the sandstones in the Xiongcun Formation. Sandstone data of oceanic island arc, continental island arc, andean type and passive margin are from Bhatia (1985).

over the range 50–200 μm (Fig. 7), indicating short transportation distances. These detrital zircon crystals have obvious oscillatory zones and Th/U ratios > 0.1 (Fig. 7; online Supplementary Table S1, available at http://journals.cambridge.org/geo), indicating a magmatic origin. Sample BL01-14-3, collected from the upper section of the Xiongcun Formation, yielded 109 usable $^{206}Pb/^{238}U$ ages (discordance < 20 %) in the range 161–220 Ma (Supplementary Table S1), with an age peak of *c.* 186 Ma (Fig. 8). Sample BL21-06-05, from the lower section of the Xiongcun Formation, yielded 132 usable $^{206}Pb/^{238}U$ ages (discordance < 20 %) in the range 191–243 Ma (Supplementary Table S1), with the peak centred at *c.* 211 Ma (Fig. 8).

4.d. *In situ* zircon Hf isotopes

A total of 69 relatively large detrital zircon grains from the sandstone samples BL01-14-3 (n = 30) and BL21-06-05 (n = 39) were analysed for *in situ* Hf isotopic abundance (Fig. 7; online Supplementary Table S2, available at http://journals.cambridge.org/geo). The $\varepsilon_{Hf}(t)$ values of sample BL01-14-3 vary from 10.45 to 16.21 (Fig. 9), with T_{DM1} model ages in the range 170–404 Ma and T_{DM2} model ages in the range 162–526 Ma. The $\varepsilon_{Hf}(t)$ values of sample BL21-06-05 vary from 10.80 to 15.96 (Fig. 9), with T_{DM1} model ages in the range 215–419 Ma and T_{DM2} model ages in the range 210–529 Ma.

5. Discussion

5.a. Volcanism-sedimentation age of the Xiongcun Formation

The youngest U–Pb age of zircon grains in populations of detrital zircons can roughly reflect the depositional age, although it should not be applied to precisely constrain maximum depositional ages of stratigraphic units (Surpless *et al.* 2006; Brown & Gehrels, 2007; Dickinson & Gehrels, 2009; Gehrels, 2015). On the other hand, minimum volcanism-sedimentation ages can be constrained by cross-cutting intrusive rocks. We therefore utilized the ages of volcanic and intrusive rocks coupled with the youngest single-grain U–Pb ages from the sandstone samples to constrain a permissible period for deposition. In the lower section of Xiongcun Formation, sandstone sample BL21-06-05 yielded a youngest detrital zircon $^{206}Pb/^{238}U$

https://doi.org/10.1017/S0016756818000122 Published online by Cambridge University Press

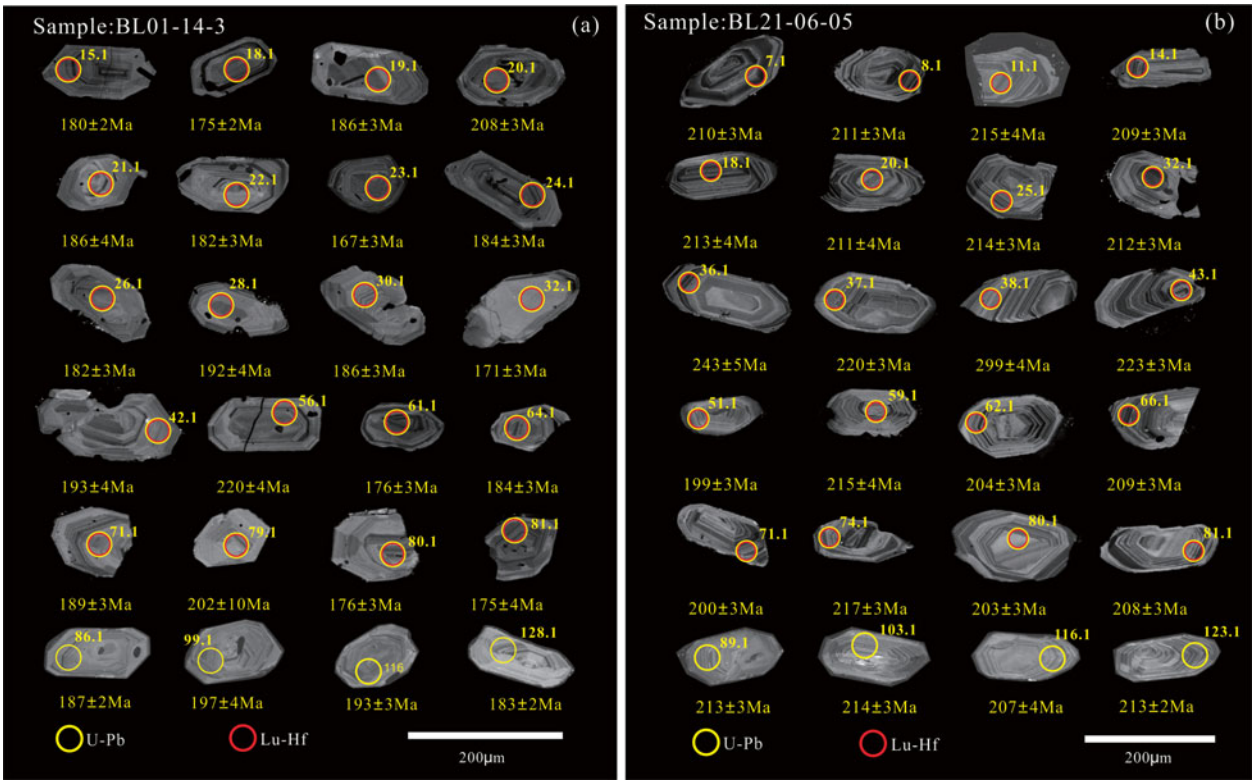

Figure 7. (Colour online) Representative cathodoluminescence (CL) images of detrital zircons from the sandstones in the Xiongcun Formation.

age of 191 ± 3 Ma (Supplementary Table S1), suggesting that the initial deposition of sandstones from the lower section of Xiongcun Formation likely occurred after 191 Ma. Qu *et al.* (2007*b*) obtained a SHRIMP zircon U–Pb age of 195 ± 4.6 Ma from a dacite in the lower section of the Xiongcun Formation (Fig. 3); the lower section of Xiongcun Formation therefore probably formed during the Early Jurassic period. For the upper section of Xiongcun Formation, Tang *et al*. (2010) reported a LA-ICP-MS zircon U–Pb age of 176 ± 5 Ma from tuff (Fig. 3). Sandstone sample BL01-14-3 yielded a youngest detrital zircon $^{206}Pb/^{238}U$ age of 161 ± 2 Ma (Supplementary Table S1), indicating deposition likely occurred after 161 Ma. However, the upper section of Xiongcun Formation was intruded by the 165.3 ± 1.0 Ma diabase dykes (Fig. 3; Lang *et al.* 2017). This inconsistent feature can probably be ascribed to the fact that the youngest U–Pb age of detrital zircon grains does not reliably constrain the maximum depositional age of stratigraphic units (Dickinson & Gehrels, 2009). According to the age of the diabase dykes, we propose that the upper section of Xiongcun Formation probably formed during Middle Jurassic time. In summary, we interpret that the Xiongcun Formation formed during the Early–Middle Jurassic period (195–165 Ma).

5.b. Weathering

The alteration of rocks during weathering results in the depletion of alkali and alkaline Earth elements and preferential enrichment of Al_2O_3 in sediments (Sun, Gui & Chen, 2012). The weathering history of ancient sedimentary rocks can therefore be partly evaluated by examining relationships among the alkali and alkaline Earth elements (Nesbitt & Young, 1982), and the chemical indexes of CIA and CIW (Nesbitt & Young, 1982; Cullers, 2000) are widely used to identify the chemical weathering intensity of a source area. The high CIA and CIW values (Table 2) of the sandstones from the Xiongcun Formation indicate moderate to high weathering and tropical conditions in the source area during the Late Triassic – Jurassic period (Nesbitt & Young, 1982). In the A (Al_2O_3) – CN ($CaO^* + Na_2O$) – K (K_2O) diagram (Fig. 10), which is useful for examining weathering and evaluating fresh rock compositions (Nesbitt & Young, 1982, 1989; Fedo, Nesbitt & Young, 1995), the sandstone samples show moderate to intensive weathering and a felsic and intermediate igneous provenance (andesite, granodiorite and granite). To summarize, the source weathering condition of the sandstones from the Xiongcun Formation is similar to a modern tropical climate. This is supported by the palaeogeography of the Lhasa terrane that suggests a location near the equator during the Late Triassic – Jurassic period (Metcalfe, 2006).

5.c. Provenance

Modal abundance, whole-rock chemistry, and zircon U–Pb and Lu–Hf isotopes can provide useful constraints for the provenance of sandstones (Dickinson

https://doi.org/10.1017/S0016756818000122 Published online by Cambridge University Press

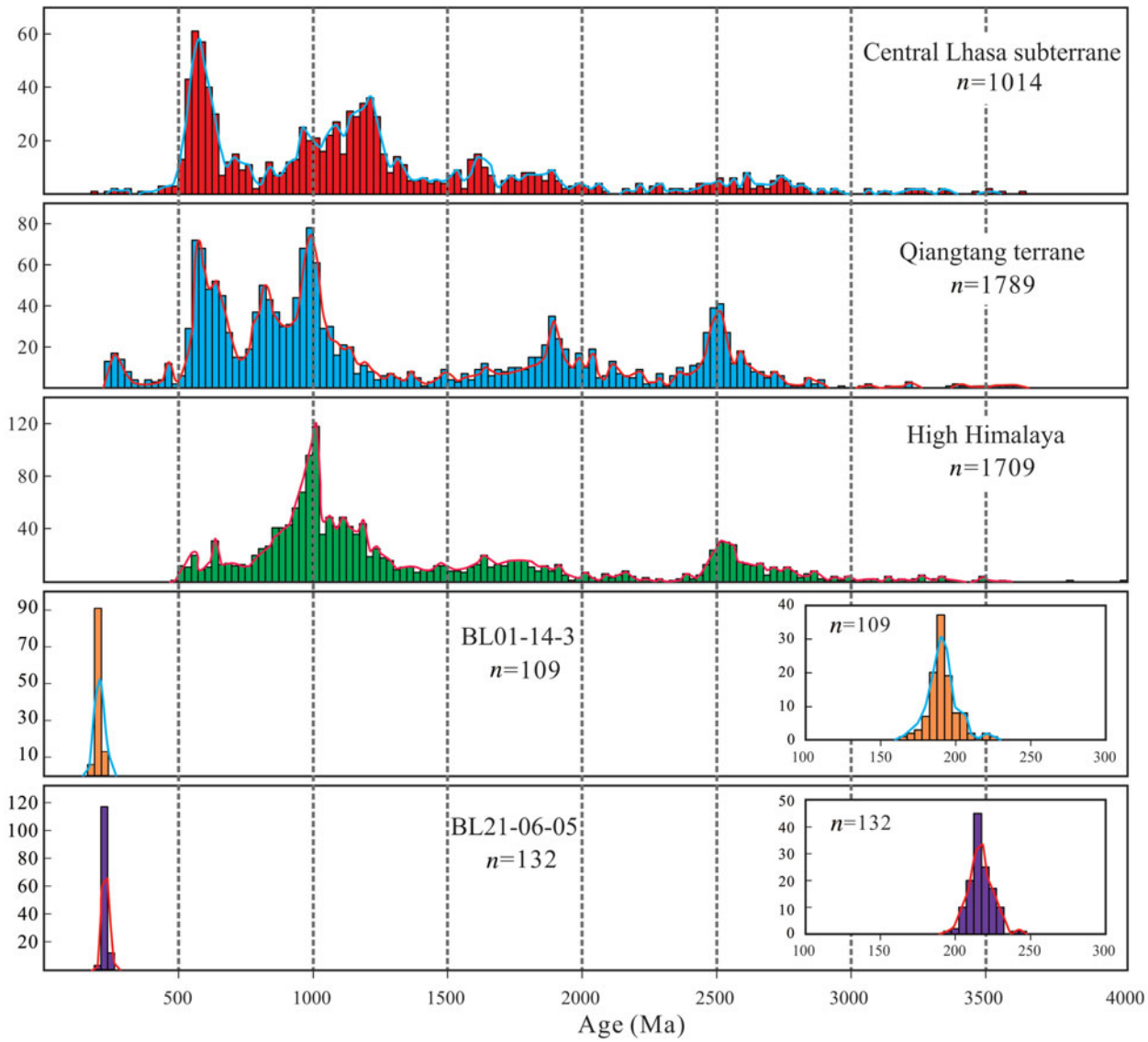

Figure 8. (Colour online) Detrital zircon age distribution from the sandstones in the Xiongcun Formation and relevant regions. Data sources: central Lhasa subterrane (Leier *et al.* 2007; Pullen *et al.* 2008*a*; Gehrels *et al.* 2011; Zhu *et al.* 2011*a*), Qiangtang terrane (Pullen *et al.* 2008*b*, 2011; Dong *et al.* 2011; Gehrels *et al.* 2011; Zhu *et al.* 2011*a*) and High Himalaya (Gehrels *et al.* 2006, 2011; McQuarrie *et al.* 2008; Myrow *et al.* 2009, 2010).

& Suczek, 1979; Bhatia, 1983; McLennan *et al.* 1993; Griffin *et al.* 2004; Han *et al.* 2012; Sun, Gui & Chen, 2012; Chen *et al.* 2016). Detrital zircons of sandstone from the Xiongcun Formation are typically prismatic crystals with oscillatory zoning (Fig. 7), indicating that these zircons are magmatic in origin and were likely derived from the contemporaneous igneous rocks in the region, a proximal source. Modal abundance shows that the provenance of the sandstones was mainly a magmatic arc (Fig. 5b). The Th–Hf–Co discrimination diagram proposed by Taylor & McLennan (1985) also supports a magmatic arc provenance (Fig. 5c). In the A–CN–K diagram (Fig. 10), the sandstones show a felsic and intermediate igneous provenance. In the F1 versus F2 discrimination diagram (Fig. 11a), the analysed data also plot in the felsic and intermediate igneous provenance fields. Again, the Al_2O_3 versus TiO_2 diagram shows that the sandstones are of felsic and intermediate igneous provenance (Fig. 11b). In addition, in the trace-element plot of La/Sc versus Co/Th (Fig. 11c), the data display high Co/Th ratios and low La/Sc ratios, dominantly indicating andesitic source rocks. Similarly, in the Hf versus La/Th diagram (Fig. 11d), the data fall within the mixed felsic-basic source and andesitic arc source fields.

Detrital zircon age data indicate that the Jurassic sandstones from the Xiongcun Formation received detritus from sources of age 161–243 Ma. Ages in this range have been reported for igneous rocks in the central and southern Lhasa subterranes (Chu *et al.* 2006; Zhang *et al.* 2007; Ji *et al.* 2009; Zhu *et al.* 2009, 2011*b*). However, detrital zircons from the Jurassic sandstones in the Xiongcun district show high and positive $\varepsilon_{Hf}(t)$ values (10.45–16.21), indicating that they are probably derived from igneous rocks in the southern Lhasa subterrane rather than the central Lhasa

https://doi.org/10.1017/S0016756818000122 Published online by Cambridge University Press

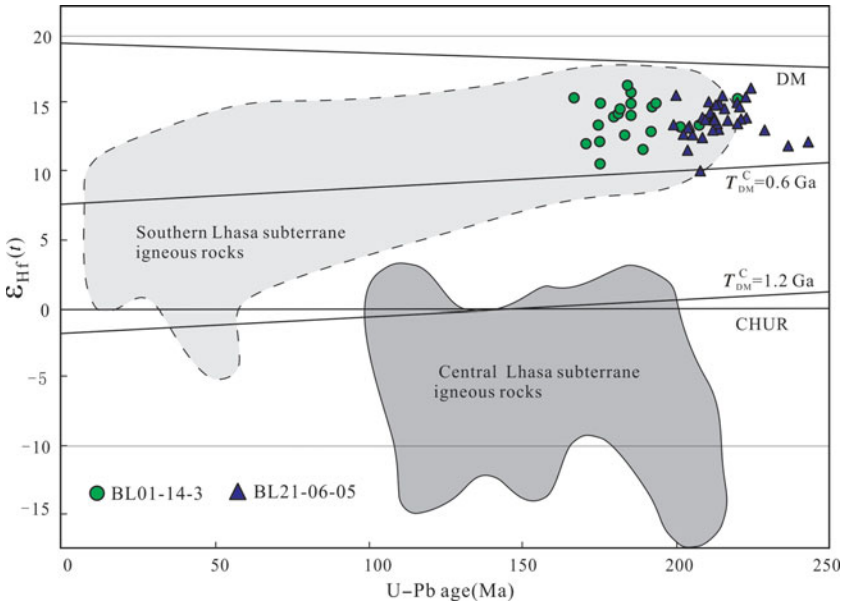

Figure 9. (Colour online) U–Pb ages versus $\varepsilon_{Hf}(t)$ values of the detrital zircons from the sandstones in the Xiongcun Formation. Southern Lhasa subterrane igneous rocks after Ji *et al.* (2009) and central Lhasa subterrane igneous rocks after Zhu *et al.* (2009, 2011*b*).

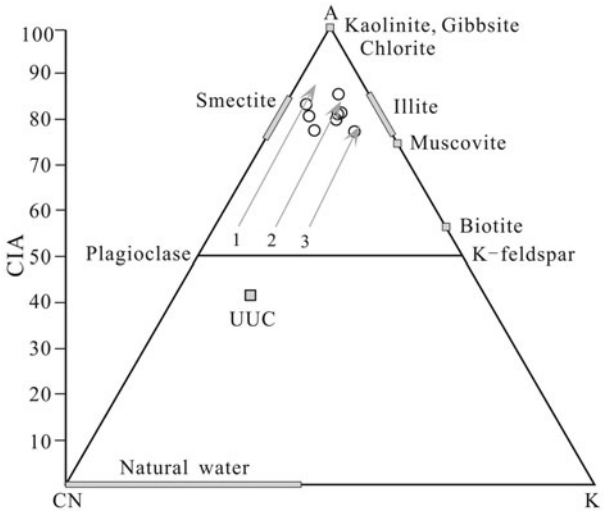

Figure 10. A–CN–K diagram for the sandstones in the Xiongcun Formation (after Nesbitt & Young, 1984). Arrows 1–3 represent the weathering trends of andesite, granodiorite and granite, respectively.

subterrane (Fig. 9). The Triassic and Jurassic igneous rocks in the southern Lhasa subterrane have been attributed to the northwards subduction of the Neo-Tethys oceanic slab (Chu *et al.* 2006; Zhang *et al.* 2007; Qu *et al.* 2007*b*; Ji *et al.* 2009; Tang *et al.* 2010; Guo *et al.* 2013; Lang *et al.* 2014; Qiu *et al.* 2015; Meng *et al.* 2016*a*, *b*). This is consistent with the modal abundance and whole-rock chemistry findings that the sandstones from the Xiongcun Formation are derived from felsic and intermediate igneous rocks in a magmatic arc. Furthermore, detrital zircon ages from the sandstones in the Xiongcun Formation lack the typical ages from the central Lhasa subterrane (age peaks of *c.* 600, 1200, 1600 and 2700 Ma), the Qiangtang terrane (age peaks of *c.* 600, 800, 1000 and 2500 Ma) and the High Himalaya (age peaks of *c.* 1000, 1700 and 2600 Ma) (Fig. 8), probably suggesting a lack of provenance from the central Lhasa subterrane, the Qiangtang terrane and the High Himalaya. On the other hand, the fact that the southern Lhasa subterrane is characterized by an absence of ancient, evolved basement rocks and is composed of juvenile crust (Hou *et al.* 2015*a*) further supports the interpretation that the local provenance of the Jurassic sandstones in the Xiongcun Formation lacks old basement components. In summary, the sandstones from the Xiongcun Formation were likely derived from Triassic and Jurassic subduction-related felsic and intermediate igneous rock in the southern Lhasa subterrane.

5.d. Tectonic settings

Sandstones can be formed in tectonic settings such as oceanic island arcs, continental island arcs, active continental margins and passive margins (Bhatia, 1983, 1985; Bhatia & Crook, 1986). The studies of Bhatia (1983) have shown that there is an increase in TiO_2, $Fe_2O_3^* + MgO$ and Al_2O_3/SiO_2 as the tectonic setting changes from the passive margin type (average TiO_2 = 0.49 %, $Fe_2O_3^* + MgO$ = 2.89 %, Al_2O_3/SiO_2 = 0.10), to an active continental margin (average TiO_2 = 0.46 %, $Fe_2O_3^* + MgO$ = 4.63 %, Al_2O_3/SiO_2 = 0.18), to a continental island arc (average TiO_2 = 0.64 %, $Fe_2O_3^* + MgO$ = 6.79 %, Al_2O_3/SiO_2 = 0.20) to an oceanic island arc (average TiO_2 = 1.06 %, $Fe_2O_3^* + MgO$ = 11.73 %, Al_2O_3/SiO_2 = 0.29). The sandstones from the Xiongcun Formation are characterized by high contents of TiO_2 and $Fe_2O_3^* + MgO$ and high Al_2O_3/SiO_2 ratios (Table 2), which are similar to the major-element characteristics of sandstones

https://doi.org/10.1017/S0016756818000122 Published online by Cambridge University Press

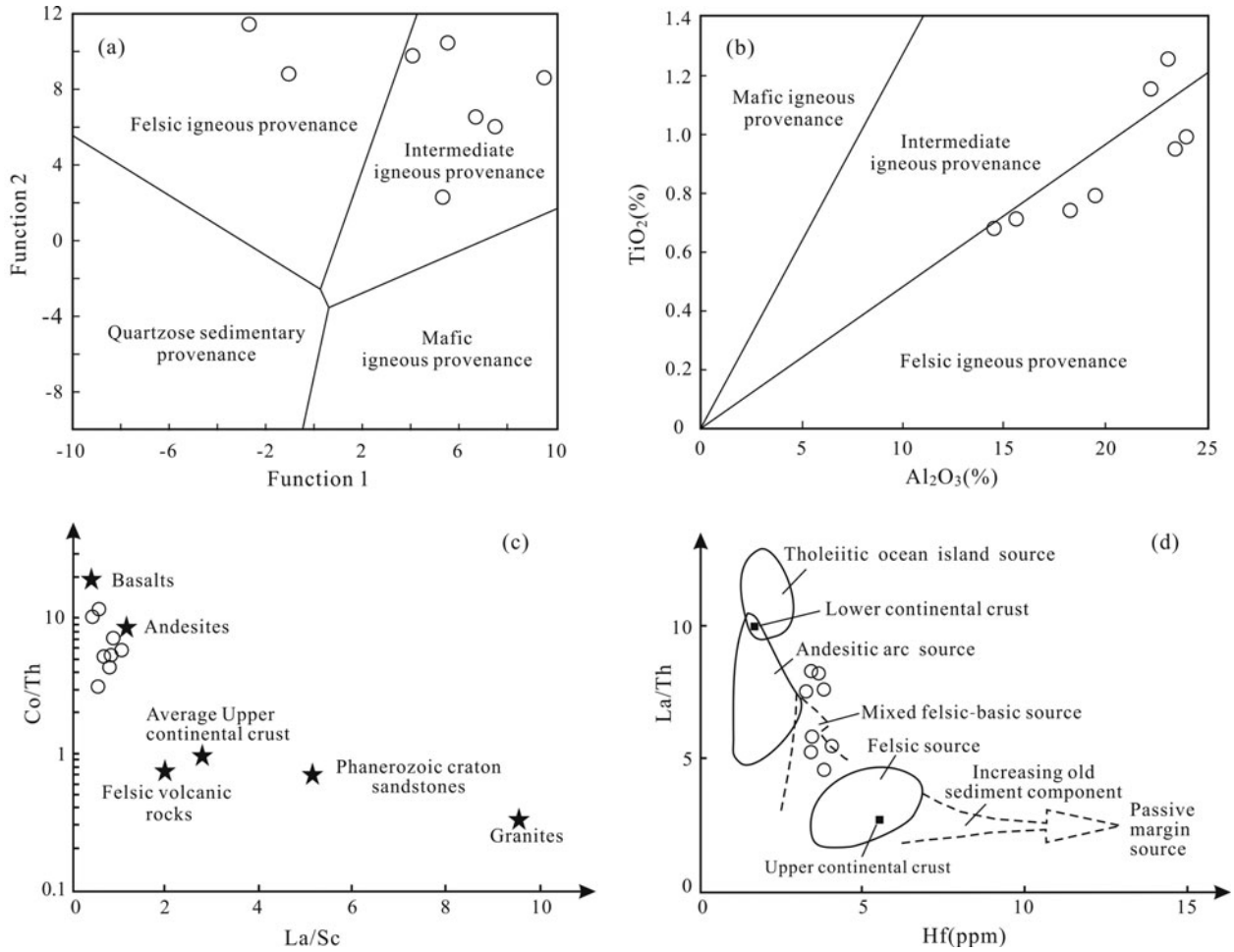

Figure 11. (a) Discriminant function diagram (after Roser & Korsch, 1988); (b) Al_2O_3 versus TiO_2 diagram (after Hayashi *et al.* 1997); (c) La/Sc versus Co/Th diagram (after Gu *et al.* 2002); and (d) Hf versus La/Th diagram (after Floyd & Leveridge, 1987) for the sandstones in the Xiongcun Formation.

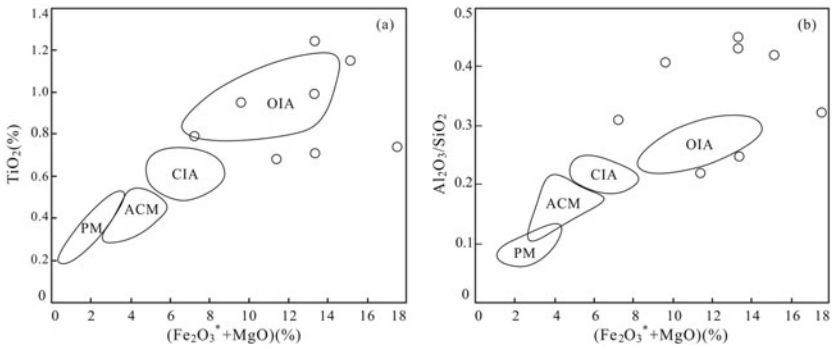

Figure 12. Tectonic setting discrimination diagrams of (a) $(Fe_2O_3^* + MgO)$ v. TiO_2 and (b) $(Fe_2O_3^* + MgO)$ v. Al_2O_3/SiO_2 for the sandstones in the Xiongcun Formation (after Bhatia, 1983). OIA – oceanic island arc; CIA – continental island arc; ACM – active continental margin; PM – passive margin.

from an oceanic island-arc setting (Bhatia, 1983). In addition, in the $(Fe_2O_3^* + MgO)$ versus TiO_2 and $(Fe_2O_3^* + MgO)$ versus (Al_2O_3/SiO_2) diagrams (Fig. 12), the sandstone samples plot near the oceanic island-arc field, again suggesting that they probably formed in an oceanic island-arc setting.

The REE characteristics of sandstones are also used to discriminate among tectonic settings (Winchester & Max, 1989). In chondrite-normalized REE patterns (Fig. 6a) and PAAS-normalized REE patterns (Fig. 6b), the REE characteristics of the sandstones from the Xiongcun Formation are consistent with those of an oceanic island-arc setting. Immobile trace elements have additionally been used to successfully discriminate among the tectonic settings of clastic sediments (Bhatia & Crook, 1986; McLennan *et al.* 1993;

https://doi.org/10.1017/S0016756818000122 Published online by Cambridge University Press

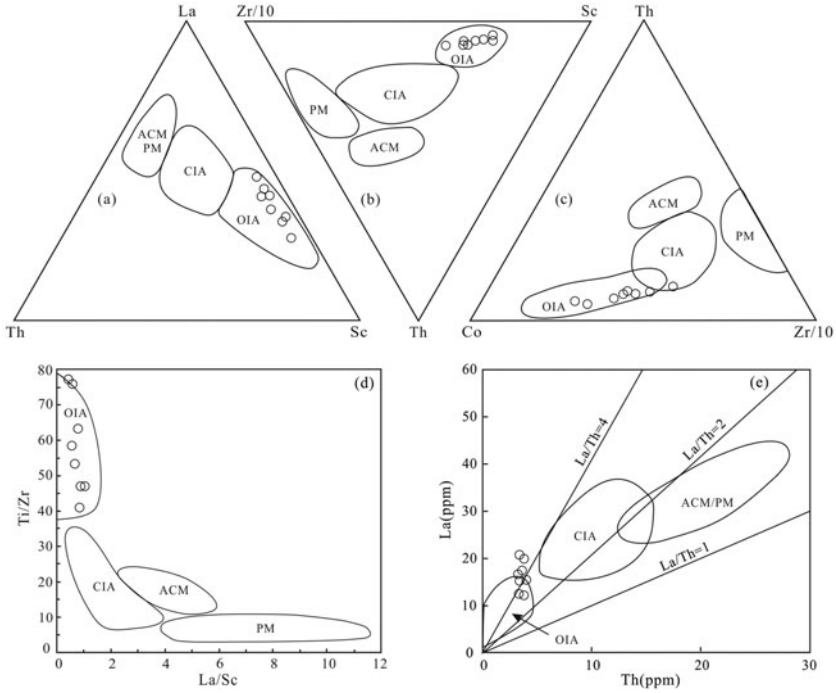

Figure 13. Tectonic setting discrimination diagrams of (a) La–Th–Sc, (b) Th–Sc–Zr/10, (c) Th–Co–Zr/10, (d) La/SC versus Ti/Zr and (e) Th versus La for the sandstones in the Xiongcun Formation (after Bhatia & Crook, 1986). Abbreviations as for Figure 12.

Griffin *et al.* 2004; Sun, Gui & Chen, 2012; Shi *et al.* 2016). The Jurassic sandstones in the Xiongcun district show: low abundances of La, Th, Zr and Nb; low ratios of Th/U and La/Sc; and high ratios of La/Th and Zr/Th (Table 2). These trace-element characteristics are very similar to those of sandstones from an oceanic island-arc setting (Bhatia & Crook, 1986). On the La–Th–Sc, Th–Sc–Zr/10 and Th–Co–Zr/10 diagrams proposed by Bhatia & Crook (1986), all the sandstones were plotted in the oceanic island-arc fields (Fig. 13a–c). In the La/Sc versus Ti/Zr and Th versus La diagrams proposed by Bhatia & Crook (1986), all the samples also fall into the oceanic island-arc fields (Fig. 13d-e).

The detrital zircon U–Pb ages of the sandstones from the Xiongcun Formation range over 161–243 Ma (Supplementary Table S1; Figs 7, 8), which obviously lack older zircons from adjacent crustal domains such as the central Lhasa subterrane, the Qiangtang terrane and the High Himalaya (Fig. 8). This indicates that the sandstones most likely formed in an oceanic island arc rather than a continental island arc. Similarly, the Jurassic igneous rocks in the Xiongcun porphyry copper–gold district were also interpreted to have been generated within an oceanic island-arc system (Tang *et al.* 2015; Lang *et al.* 2017; Ma *et al.* 2017*b*; Yin *et al.* 2017).

We suggest that the tectonic setting of the sandstone from the Xiongcun Formation was probably an oceanic island-arc setting (Fig. 14). Our data support the opinion that the southern Lhasa subterrane was likely an oceanic island-arc setting rather than a continental island-arc setting during the Late Triassic–Jurassic period.

6. Conclusions

Based on petrology, geochemistry, zircon U–Pb dating and Lu–Hf results from Jurassic sandstones of the Xiongcun Formation in the Xiongcun district, we can draw the following conclusions.

(1) The sandstones of Xiongcun Formation formed during Early–Middle Jurassic time (195–165 Ma). The sandstones are exposed in the lower and upper sections of the Xiongcun Formation. These sandstones mainly contain $L_{63–70}$ (lithic fragments), $Q_{18–28}$ (monocrystalline and polycrystalline quartz) and $F_{8–12}$ (alkali feldspar and plagioclase), indicating that they can be classified as lithic arenite. The high CIA values (77.19–85.36, mean 79.96) and CIW values (86.19–95.59, mean 89.98) of the sandstones imply moderate to high weathering and tropical climate conditions in the source area.

(2) Framework petrography, major oxides and trace elements indicate that these sandstones were derived from felsic and intermediate igneous rocks, probably with a magmatic-arc provenance. Detrital zircon ages and $\varepsilon_{Hf}(t)$ values further constrain the sandstones provenance as Triassic and Jurassic subduction-related felsic and intermediate igneous rocks in the southern Lhasa subterrane. The tectonic setting discrimination diagrams, as well as the chemical compositions and detrital zircon ages, support an oceanic island-arc setting for the sandstones from the Xiongcun Formation.

(3) The geologic setting of the southern Lhasa subterrane during the Late Triassic – Jurassic period was probably an oceanic island-arc setting rather than a continental island-arc setting.

https://doi.org/10.1017/S0016756818000122 Published online by Cambridge University Press

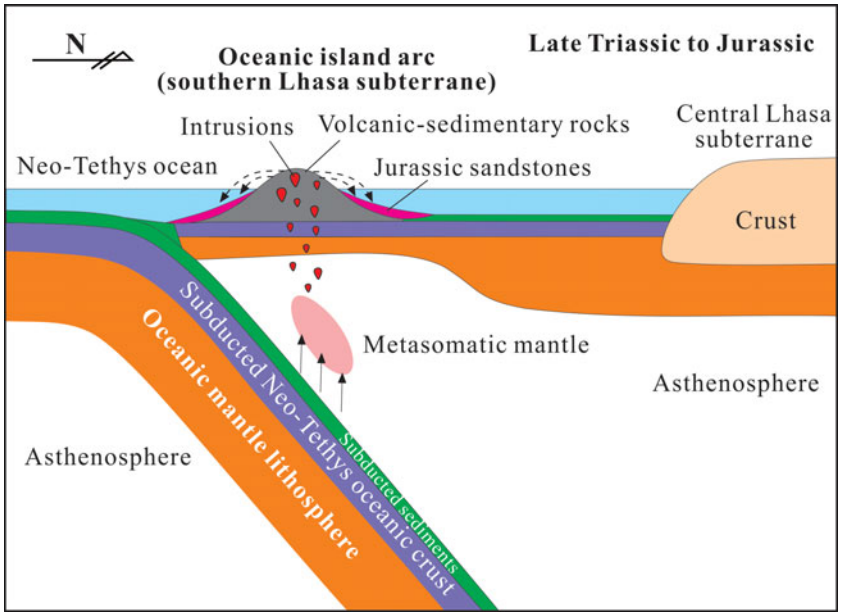

Figure 14. (Colour online) Schematic diagram showing provenance and tectonic setting of the sandstones in the Xiongcun Formation (modified from Tang et al. 2015).

Acknowledgements. This research was jointly supported by the National Science Foundation of China (41502079), State Key Laboratory of Continental Tectonics and Dynamics (K201401), State Key Laboratory of Ore Deposit Geochemistry (201503), State Key Laboratory for Mineral Deposits Research (2017-LAMD-K04), Special Scientific Research Fund of Public Welfare Profession of MLR, China (201511022-05) and Sichuan Youth Science and Technology Foundation (2014JQ0047). We are grateful to Dr Andrew Laskowski and the other anonymous reviewer for their constructive comments, which greatly improved the manuscript.

Supplementary material

To view supplementary material for this article, please visit https://doi.org/10.1017/S0016756818000122

References

Ahmad, T., Tanaka, T., Sachan, H. K., Asahara, Y., Islam, R. & Khanna, P. P. 2008. Geochemical and isotopic constraints on the age and origin of the Nidar Ophiolitic Complex, Ladakh, India: Implications for the Neo-Tethyan subduction along the Indus suture zone. *Tectonophysics* **451**(1–4), 206–24.

Aitchison, J. C., Ali, J. R. & Davis, A. M. 2007. When and where did India and Asia collide? *Journal of Geophysical Research* **112**. B05423.

Andersen, T. 2002. Correction of common lead in U–Pb analyses that do not report ^{204}Pb. *Chemical Geology* **192**(1), 59–79.

Andersen, T. 2005. Detrital zircons as tracers of sedimentary provenance: limiting conditions from statistics and numerical simulation. *Chemical Geology* **216**, 249–70.

Augustsson, C., Münker, C., Bahlburg, H. & Fanning, C. M. 2006. Provenance of late Palaeozoic metasediments of the SW South American Gondwana margin: a combined U–Pb and Hf-isotope study of single detrital zircons. *Journal of the Geological Society* **163**, 983–95.

Bhatia, M. R. 1983. Plate tectonics and geochemical composition of sandstones. *Journal of Geology* **91**, 611–27.

Bhatia, M. R. 1985. Rare earth element geochemistry of Australian Paleozoic graywackes and mudrocks: provenance and tectonic control. *Sedimentary Geology* **45**(1), 97–113.

Bhatia, M. R. & Crook, K. A. 1986. Trace element characteristics of greywackes and tectonic setting discrimination of sedimentary basins. *Contributions to Mineralogy and Petrology* **92**(2), 181–93.

Black, L. P., Kamo, S. L., Allen, C. M., Aleinikoff, J. N., Davis, D. W., Korsch, R. J. & Foudoulis, C. 2003. TEMORA 1: a new zircon standard for Phanerozoic U–Pb geochronology. *Chemical Geology* **200**(1), 155–70.

Bouvier, A., Vervoort, J. D. & Patchett, P. J. 2008. The Lu–Hf and Sm–Nd isotopic composition of CHUR: constraints from unequilibrated chondrites and implications for the bulk composition of terrestrial planets. *Earth and Planetary Science Letters* **273**, 48–57.

Brown, E. R. & Gehrels, G. E. 2007. Detrital zircon constraints on terrane ages and affinities and timing of orogenic events in the San Juan Islands and North Cascades, Washington. *Canadian Journal of Earth Sciences* **44**(10), 1375–96.

Cawood, P. A., Hawkesworth, C. J. & Dhuime, B. 2012. Detrital zircon record and tectonic setting. *Geology* **40**, 875–8.

Chen, Y., Zhang, Z. C., Li, K., Yu, H. F. & Wu, T. R. 2016. Detrital zircon U–Pb ages and Hf isotopes of Permo-Carboniferous sandstones in central InnerMongolia, China: implications for provenance and tectonic evolution of the southeastern Central Asian Orogenic Belt. *Tectonophysics* **671**, 183–201.

Chu, M. F., Chung, S. L., O'Reilly, S. Y., Pearson, N. J., Wu, F. Y., Li, X. H., Liu, D. Y., Ji, J. Q., Chu, C. H. & Lee, H. Y. 2011. India's hidden inputs to Tibetan orogeny revealed by Hf isotopes of Transhimalayan zircons and host rocks. *Earth and Planetary Science Letters* **307**(3), 479–86.

Chu, M. F., Chung, S. L., Song, B., Liu, D., O'Reilly, S. Y., Pearson, N. J., Ji, J. & Wen, D. J. 2006. Zircon U–Pb and Hf isotope constraints on the Mesozoic

https://doi.org/10.1017/S0016756818000122 Published online by Cambridge University Press

tectonics and crustal evolution of southern Tibet. *Geology* **34**(9), 745–8.

Chu, N. C., Taylor, R. N., Chavagnac, V., Nesbitt, R. W., Boella, R. M., Milton, J. A., Germain, C. R., Bayon, G. & Burton, K. 2002. Hf isotope ratio analysis using multicollector inductively coupled plasma mass spectrometry: an evaluation of isobaric interference corrections. *Journal of Analytical Atomic Spectrometry* **17**, 1567–74.

Chung, S. L., Chu, M. F., Zhang, Y., Xie, Y., Lo, C. H., Lee, T. Y., Lan, C.Y., Li, X. H., Zhang, Q. & Wang, Y. Z. 2005. Tibetan tectonic evolution inferred from spatial and temporal variations in post-collisional magmatism. *Earth-Science Reviews* **68**(3), 173–96.

Cullers, R. L. 2000. The geochemistry of shales, siltstones and sandstones of Pennsylvanian–Permian age, Colorado, USA: implications for provenance and metamorphic studies. *Lithos* **51**(3), 181–203.

De Bievre, P. & Taylor, P. D. P. 1993. Table of the isotopic composition of the elements. *International Journal of Mass Spectrometry and Ion Processes* **123**, 149–66.

Dickinson, W. R. 1970. Interpreting detrital modes of greywacke and arkose. *Journal of Sedimentary Petrology* **40**, 695–707.

Dickinson, W. R. 1985. Interpreting provenance relations from detrital modes of sandstones. In *Provenance of Arenites* (ed. G. G. Zuffa), pp. 333–61. NATO, Advanced Study Institute Series no. 148.

Dickinson, W. R., Beard, L. S., Brakenridge, G. R., Erjavec, J. L., Ferguson, R. C., Inman, K. F., Knepp, R. A., Lindberg, F. A. & Ryberg, P. T. 1983. Provenance of North American Phanerozoic sandstones in relation to tectonic setting. *Geological Society of America Bulletin* **94**(2), 222–35.

Dickinson, W. R. & Gehrels, G. E. 2009. Use of U–Pb ages of detrital zircons to infer maximum depositional ages of strata: a test against a Colorado plateau Mesozoic database. *Earth and Planetary Science Letters* **288**(1–2), 115–25.

Dickinson, W. R. & Suczek, C. A. 1979. Plate Tectonics and sandstone composition. *AAPG Bulletin* **63**(12), 2164–82.

Ding, L., Kapp, P. & Wan, X. Q. 2005. Paleocene–Eocene record of ophiolite obduction and initial India-Asia collision, south central Tibet. *Tectonics* **24**, 1–18.

Dong, C. Y., Li, C., Wan, Y. S., Wang, W., Wu, Y. W., Jie, K. Q. & Liu, D. Y. 2011. Detrital zircon age model of ordovician wenquan quartzite south of lungmucoshuanghu suture in the Qiangtang area, Tibet: constraint on tectonic affinity and source regions. *Science China Earth Sciences* **54**(7), 1034–42 (in Chinese with English abstract).

Du, L. L., Yang, C. H., Wyman, D. A., Nutman, A. P., Lu, Z. L., Song, H. X., Zhao, L., Geng, Y. S. & Ren, L. D. 2016. Age and depositional setting of the Paleoproterozoic Gantaohe Group in Zanhuang Complex: constraints from zircon U–Pb ages and Hf isotopes of sandstones and dacite. *Precambrian Research* **286**, 59–100.

Fedo, C. M., Nesbitt, H. W. & Young, G. M. 1995. Unraveling the effects of potassium metasomatism in sedimentary rocks and paleosols, with implications for paleoweathering conditions and provenance. *Geology* **23**(10), 921–4.

Floyd, P. A. & Leveridge, B. E. 1987. Tectonic environment of the Devonian Gramscatho basin, south Cornwall: framework mode and geochemical evidence from turbiditic sandstones. *Journal of the Geological Society* **144**(4), 531–42.

Gazzi, P. 1966. Le arenarie del flysch sopracretaceo dell'Appennino modenese: correlazione con il flysch di Monghidoro. *Mineralogica et Petrographica Acta* **12**, 69–97.

Gehrels, G. E. 2015. Detrital zircon U–Pb geochronology applied to tectonics. *Annual Review of Earth and Planetary Sciences* **42**(1), 127–49.

Gehrels, G. E., Decelles, P. G., Ojha, T. P. & Upreti, B. N. 2006. Geologic and U–Pb geochronologic evidence for early Paleozoic tectonism in the Dadeldhura thrust sheet, far-west Nepal Himalaya. *Journal of Asian Earth Sciences* **28**(4–6), 385–408.

Gehrels, G. E., Kapp, P., Decelles, P., Pullen, A., Blakey, R., Weislogel, A., Ding, L., Guynn, J., Martin, A., Mcquarrie, N. & Yin, A. 2011. Detrital zircon geochronology of pre-tertiary strata in the Tibetan-Himalayan orogen. *Tectonics* **30**(5), 1–27.

Geng, Q. R., Pan, G. T., Wang, L. Q., Zhu, D. C. & Liao, Z. L. 2006. Isotopic geochronology of the volcanic rocks from the Yeba Formation in the Gangdise zone, Xizang. *Sedimentary Geology and Tethyan Geology* **26**(1), 1–7 (in Chinese with English abstract).

Griffin, W. L., Belousova, E. A., Shee, S. R., Pearson, N. J. & O'Reilly, S. Y. 2004. Archean crustal evolution in the northern Yilgarn craton: U–Pb and Hf-isotope evidence from detrital zircons. *Precambrian Research* **131**, 231–82.

Griffin, W. L., Wang, X., Jackson, S. E., Pearson, N. J., O'Reilly, S. Y., Xu, X. & Zhou, X. 2002. Zircon chemistry and magma mixing, SE China: insitu analysis of Hf isotopes, Tonglu and Pingtan igneous complexes. *Lithos* **61**, 237–68.

Gu, X. X., Liu, J. M., Zheng, M. H., Tang, J. X. & Qi, L. 2002. Provenance and tectonic setting of the Proterozoic turbidites in Hunan, South China: geochemical evidence. *Journal of Sedimentary Research* **72**(3), 393–407.

Guo, L. S., Liu, Y. L., Liu, S. W., Cawood, P. A., Wang, Z. H. & Liu, H. F. 2013. Petrogenesis of Early to Middle Jurassic granitoid rocks from the Gangdese belt, Southern Tibet: Implications for early history of the Neo-Tethys. *Lithos* **179**, 320–33.

Han, G. Q., Liu, Y. J., Neubauer, F., Genser, J., Zhao, Y., Wen, Q. B., Li, Wei., Wu, L. N., Jiang, X. Y. & Zhao, L. N. 2012. Provenance analysis of Permian sandstones in the central and southern Da Xing'an Mountains, China: constraints on the evolution of the eastern segment of the Central Asian Orogenic Belt. *Tectonophysics* **580**, 100–13.

Harnois, L. 1988. The CIW index: a new chemical index of weathering. *Sedimentary Geology* **55**, 319–22.

Hayashi, K. I., Fujisawa, H., Holland, H. D. & Ohmoto, H. 1997. Geochemistry of 1.9 Ga sedimentary rocks from northeastern Labrador, Canada. *Geochimica et Cosmochimica Acta* **61**(19), 4115–37.

He, D. F., Zhu, W. G., Zhong, H., Ren, T., Bai, Z. J. & Fan, H. P. 2013. Zircon U–Pb geochronology and elemental and Sr–Nd–Hf isotopic geochemistry of the Daocheng granitic pluton from the Yidun Arc, SW China. *Journal of Asian Earth Sciences* **67**, 1–17.

Hou, Z. Q., Duan, L. F., Lu, Y. J., Zheng, Y. C., Zhu, D. C., Yang, Z. M., Yang, Z. S., Wang, B. D., Pei, Y. R., Zhao, Z. D. & McCuaig, T. C. 2015a. Lithospheric architecture of the Lhasa Terrane and its control on ore deposits in the Himalayan-Tibetan Orogen. *Economic Geology* **110**, 1541–75.

https://doi.org/10.1017/S0016756818000122 Published online by Cambridge University Press

Hou, Z. Q., Gao, Y. F., Qu, X. M., Rui, Z. Y. & Mo, X. X. 2004. Origin of adakitic intrusives generated during mid-Miocene east–west extension in southern Tibet. *Earth and Planetary Science Letters* **220**(1), 139–55.

Hou, Z. Q., Yang, Z. M., Lu, Y. J., Kemp, A., Zheng, Y. C., Li, Q. Y., Tang, J. X., Yang, Z. S. & Duan, L. F. 2015b. A genetic linkage between subduction- and collision-related porphyry Cu deposits in continental collision zones. *Geology* **43**(3), 247–50.

Huang, F., Xu, J. F., Chen, J. L., Kang, Z. Q. & Dong, Y. H. 2015. Early Jurassic volcanic rocks from the Yeba Formation and Sangri Group: products of continental marginal arc and intra-oceanic arc during the subduction of Neo-tethys ocean? *Acta Petrologica Sinica* **31**(7), 2089–00 (in Chinese with English abstract).

Iizuka, T. & Hirata, T. 2005. Improvements of precision and accuracy in in-situ Hf isotope microanalysis of zircon using the laser ablation-MC-ICPMS technique. *Chemical Geology* **220**, 121–37.

Ji, W. Q., Wu, F. Y., Chung, S. L., Li, J. X. & Liu, C. Z. 2009. Zircon U–Pb geochronology and Hf isotopic constraints on petrogenesis of the Gangdese batholith, southern Tibet. *Chemical Geology* **262**(3), 229–45.

Kang, Z. Q., Xu, J. F., Wilde, S. A., Feng, Z. H., Chen, J. L., Wang, B. D., Fu, W. C. & Pan, H. B. 2014. Geochronology and geochemistry of the Sangri Group volcanic rocks, Southern Lhasa Terrane: implications for the early subduction history of the Neo-Tethys and Gangdese Magmatic Arc. *Lithos* **200–201**, 157–68.

Kapp, P., Decelles, P. G., Gehrels, G. E., Heizler, M. & Ding, L. 2007a. Geological records of the Cretaceous Lhasa–Qiangtang and Indo–Asian collisions in the Nima basin area, central Tibet. *Geological Society of America Bulletin* **119**, 917–32.

Kapp, P., Decelles, P. G., Leier, A. L., Fabijanic, J. M., He, S. D., Pullen, A. & Gehrels, G. E. 2007b. The Gangdese retroarc thrust belt revealed. *GSA Today* **17**(7), 4–9.

Kapp, P., Yin, A., Harrison, T. M. & Ding, L. 2005. Cretaceous–Tertiary shortening, basin development, and volcanism in central Tibet. *Geological Society America Bulletin* **117**, 865–78.

Khan, K. F., Dar, S. A. & Khan, S. A. 2012. Geochemistry of phosphate bearing sedimentary rocks in parts of Sonrai block, Lalitpur District, Uttar Pradesh, India. *Chemie der Erde – Geochemistry* **72**(2), 117–25.

Kurian, S., Nath, B. N., Kumar, N. C. & Nair, K. K. 2013. Geochemical and isotopic signatures of surficial sediments from the western continental shelf of India: inferring provenance, weathering, and the nature of organic matter. *Journal of Sedimentary Research* **83**(6), 427–42.

Lang, X. H., Tang, J. X., Li, Z. J., Dong, S. Y., Ding, F., Wang, Z. Z., Zhang, L. & Huang, Y. 2012. Geochemical evaluation of exploration prospect in the Xiongcun copper-gold district and peripheral areas, Xietongmen County, Tibet. *Geology and Exploration* **48**(1), 12–23 (in Chinese with English abstract).

Lang, X. H., Tang, J. X., Li, Z. J., Huang, Y., Ding, F., Yang, H. H., Xie, F. W., Zhang, L., Wang, Q. & Zhou, Y. 2014. U–Pb and Re–Os geochronological evidence for the Jurassic porphyry metallogenic event of the Xiongcun district in the Gangdese porphyry copper belt, southern Tibet, PRC. *Journal of Asian Earth Sciences* **79**, 608–22.

Lang, X. H., Wang, X. H., Tang, J. X., Deng, Y. L., Cui, Z. W., Yin, Q. & Xie, F, W. 2017. Composition and age of Jurassic diabase dikes in the Xiongcun porphyry copper–gold district, southern margin of the Lhasa terrane, Tibet, China: petrogenesis and tectonic setting. *Geological Journal*, published online 20 October 2017. doi: 10.1002/gj.3028.

Lee, H. Y., Chung, S. L., Lo, C. H., Ji, J., Lee, T. Y., Qian, Q. & Zhang, Q. 2009. Eocene Neotethyan slab breakoff in southern Tibet inferred from the Linzizong volcanic record. *Tectonophysics* **477**(1), 20–35.

Leier, A. L., Paul, K., Gehrels, G. E. & Decelles, P. G. 2007. Detrital zircon geochronology of Carboniferous–Cretaceous strata in the Lhasa terrane, Southern Tibet. *Basin Research* **19**(3), 361–78.

Li, C. S., Arndt, N. T., Tang, Q. Y. & Ripley, E. M. 2015. Trace element indiscrimination diagrams. *Lithos* **232**, 76–83.

Li, J. X., Qin, K. Z., Li, G. M., Xiao, B., Chen, L. & Zhao, J. X. 2011. Post-collisional ore-bearing adakitic porphyries from Gangdese porphyry copper belt, southern Tibet: melting of thickened juvenile arc lower crust. *Lithos* **126**(3), 265–77.

Ma, S. W., Meng, Y. K., Xu, Z. Q. & Liu, X. J. 2017a. The discovery of Late Triassic mylonitic granite and geologic significance in the middle Gangdese batholiths, southern Tibet. *Journal of Geodynamics* **104**, 49–64.

Ma, X. X., Xu, Z. Q., Meert, J. & Santosh, M. 2017b. Early Jurassic intra-oceanic arc system of the Neotethys Ocean: Constraints from andesites in the Gangdese magmatic belt, south Tibet. *Island Arc*, published online 30 June 2017. doi: 10.1111/iar.12202.

Ma, X. X., Yi, Z. Y. & Xu, Z. Q. 2017. Late Triassic intraoceanic arc aystem within Neotethys: evidence from cumulate hornblende gabbro in Gangdese Belt, South Tibet. *Acta Geologica Sinica (English Edition)* **91**(S1), 21.

Mahéo, G., Bertrand, H., Guillot, S., Villa, I. M., Keller, F. & Capiez, P. 2004. The South Ladakh Ophiolites (NW Himalaya, India): an intra-oceanic tholeiitic arc origin with implication for the closure of the Neo-Tethys. *Chemical Geology* **203**(3), 273–303.

McDermid, I. R., Aitchison, J. C., Davis, A. M., Harrison, T. M. & Grove, M. 2002. The Zedong terrane: a Late Jurassic intra-oceanic magmatic arc within the Yarlung-Tsangpo suture zone, southeastern Tibet. *Chemical Geology* **187**, 267–77.

McLennan, S. M. 1993. Weathering and global denudation. *The Journal of Geology* **101**, 295–303.

McLennan, S. M., Hemming, S., McDaniel, D. K. & Hanson, G. N. 1993. Geochemical approaches to sedimentation, provenance, and tectonics. *Special Paper of the Geological Society of America* **284**, 21–40.

McLennan, S. M. & Taylor, S. R. 1991. Sedimentary rocks and crustal evolution: tectonic setting and secular trends. *Journal of Geology* **99**(1), 1–21.

McQuarrie, N., Robinson, D., Long, S., Tobgay, T., Grujic, D., Gehrels, G. & Ducea, M. 2008. Preliminary stratigraphic and structural architecture of Bhutan: implications for the along strike architecture of the Himalayan system. *Earth and Planetary Science Letters* **272**(1), 105–17.

Meng, Y. K., Dong, H. W., Cong, Y., Xue, Z.Q. & Cao, H. 2016a. The early-stage evolution of the Neo-Tethys ocean: evidence from granitoids in the middle Gangdese batholith, southern Tibet. *Journal of Geodynamics* **94–95**, 34–49.

Meng, Y. K., Xu, Z. Q., Santosh, M., Ma, X. X., Chen, X. J., Guo, G. L. & Liu, F. 2016b. Late Triassic crustal growth in southern Tibet: evidence from the Gangdese magmatic belt. *Gondwana Research* **37**, 449–64.

https://doi.org/10.1017/S0016756818000122 Published online by Cambridge University Press

Metcalfe, I. 2006. Palaeozoic and Mesozoic tectonic evolution and palaeogeography of East Asian crustal fragments: the Korean Peninsula in context. *Gondwana Research* **9**(1–2), 24–46.

Mo, X. X., Dong, G. C., Zhao, Z. D., Guo, T. Y., Wang, L. L. & Chen, T. 2005a. Timing of magma mixing in the Gangdise magmatic belt during the India-Asia collision: zircon SHRIMP U–Pb dating. *Acta Geologica Sinica (English Edition)* **79**(1), 66–76.

Mo, X. X., Dong, G. C., Zhao, Z. D., Zhou, S., Wang, L. L., Qiu, R. Z. & Zhang, F. Q. 2005b. Spatial and temporal distribution and characteristics of granitoids in the Gangdese, Tibet and implication for crustal growth and evolution. *Geological Journal of China Universities* **11**(3), 281–90 (in Chinese with English abstract).

Mo, X. X., Niu, Y. L., Dong, G. C., Zhao, Z. D., Hou, Z. Q., Zhou, S. & Ke, S. 2008. Contribution of syncollisional felsic magmatism to continental crust growth: a case study of the Paleogene Linzizong volcanic succession in southern Tibet. *Chemical Geology* **250**(1), 49–67.

Mo, X. X., Zhao, Z. D., Deng, J. F., Dong, G. C., Zhou, S., Guo, T. Y., Zhang, S. L. & Wang, L. L. 2003. Response of volcanism to the India-Asia collision. *Earth Science Frontiers* **10**(3), 135–48 (in Chinese with English abstract).

Myrow, P. M., Hughes, N. C., Goodge, J. W., Fanning, C. M., Williams, I. S., Peng, S. C., Bhargava, O. N., Parcha, S. K. & Pogue, K. R. 2010. Extraordinary transport and mixing of sediment across Himalayan central Gondwana during the Cambrian-Ordovician. *Geological Society of America Bulletin* **122**(9), 1660–70.

Myrow, P. M., Hughes, N. C., Searle, M. P., Fanning, C. M., Peng, S. C. & Parcha, S. K. 2009. Stratigraphic correlation of Cambrian-Ordovician deposits along the Himalaya: implications for the age and nature of rocks in the Mount Everest region. *Geological Society of America Bulletin* **121**(3–4), 323–32.

Nesbitt, H. W. & Young, G. M. 1982. Early Proterozoic climates and plate motions inferred from major element chemistry of lutites. *Nature* **299**(5885), 715–7.

Nesbitt, H. W. & Young, G. M. 1984. Prediction of some weathering trends of plutonic and volcanic rocks based on thermodynamic and kinetic considerations. *Geochimica et Cosmochimica Acta* **48**(7), 1523–34.

Nesbitt, H. W. & Young, G. M. 1989. Formation and diagenesis of weathering profiles. *The Journal of Geology* **97**(2), 129–47.

Okada, H. 1971. Classification of sandstones: analysis and proposals. *Journal of Geology* **79**, 509–25.

Osae, S., Asiedu, D. K., Banoeng-Yakubo, B., Koeberl, C. & Dampare, S. B. 2006. Provenance and tectonic setting of Late Proterozoic Buem sandstones of southeastern Ghana: Evidence from geochemistry and detrital modes. *Journal of African Earth Sciences* **44**, 85–96.

Pan, G. T., Mo, X. X., Zhu, D. C., Wang, L. Q., Li, G. M., Zhao, Z. D., Geng, Q. R. & Liao, Z. L. 2006. Spatial-temproral framework of the orogenic belt and its evolution. *Acta Petrologica Sinica* **22**(3), 521–33 (in Chinese with English abstract).

Pullen, A., Kapp, P., Gehrels, G. E., Decelles, P. G., Brown, E. H., Fabijanic, J. M. & Ding, L. 2008*a*. Gangdese retroarc thrust belt and foreland basin deposits in the Damxung area, southern Tibet. *Journal of Asian Earth Sciences* **33**(5–6), 323–36.

Pullen, A., Kapp, P., Gehrels, G. E., Ding, L. & Zhang, Q. 2011. Metamorphic rocks in central Tibet: Lateral variations and implications for crustal structure. *Geological Society of America Bulletin* **123**(3–4), 585–600.

Pullen, A., Kapp, P., Gehrels, G. E., Vervoort, J. D. & Ding, L. 2008b. Triassic continental subduction in central Tibet and Mediterranean-style closure of the Paleo-Tethys Ocean. *Geology* **36**(5), 351–4.

Qi, L., Hu, J. & Grégoire, D. C. 2000. Determination of trace elements in granites by inductively coupled plasma mass spectrometry. *Talanta* **51**(3), 507–13.

Qiu, J. S., Wang, R. Q., Zhao, J. L. & Yu, S. B. 2015. Petrogenesis of the Early Jurassic gabbro-granite complex in the middle segment of gangdese belt and its implication for tectonic evolution of Neo-tethys: a case study of the Dongga pluton in Xigaze. *Acta Petrologica Sinica* **31**(12), 3569–80 (in Chinese with English abstract).

Qu, X. M., Hou, Z. Q., Zaw, K. & Li, Y. G. 2007a. Characteristics and genesis of Gangdese porphyry copper deposits in the southern Tibetan Plateau: Preliminary geochemical and geochronological results. *Ore Geology Reviews* **31**(1), 205–23.

Qu, X. M., Xin, H. B. & Xu, W. Y. 2007b. Collation of age of ore-hosting volcanics in Xiongcun superlarge Cu-Au deposit on basis of three zircon U–Pb SHRIMP ages. *Mineral Deposits* **26**(5), 512–8 (in Chinese with English abstract).

Rolland, Y., Pêcher, A. & Picard, C. 2000. Middle Cretaceous back-arc formation and arc evolution along the Asian margin: the Shyok Suture Zone in northern Ladakh (NW Himalaya). *Tectonophysics* **325**(1–2), 145–73.

Roser, B. P. & Korsch, R. J. 1988. Provenance signatures of sandstone-mudstone suites determined using discriminant function analysis of major-element data. *Chemical Geology* **67**(1), 119–39.

Shi, G. Z., Wang, H., Huang, C. Y., Yang, S. Y. & Song, G. Z. 2016. Provenance and tectonic setting of middle-upper Devonian sandstones in the Qinling Orogen (Shanyang area): new insights from geochemistry, heavy minerals and tourmaline chemistry. *Tectonophysics* **688**, 11–25.

Söerlund, U., Patchett, P. J., Vervoort, J. D. & Isachsen, C. E. 2004. The ^{176}Lu decay constant determined by Lu–Hf and U–Pb isotope systematics of Precambrian mafic intrusions. *Earth and Planetary Science Letters* **219**, 311–24.

Sun, L. H., Gui, H. R. & Chen, S. 2012. Geochemistry of sandstones from the Neoproterozoic Shijia Formation, northern Anhui Province, China: implications for provenance, weathering and tectonic setting. *Chemie der Erde-Geochemistry* **72**(3), 253–60.

Sun, S. S. & McDonough, W. S. 1989. Chemical and isotopic systematics of oceanic basalts: implications for mantle composition and processes. In *Magmatism in the Ocean Basins* (eds A. D. Saunders & M. J. Norry), pp. 313–45. Geological Society, London, Special Publication no. 42.

Surpless, K. D., Graham, S. A., Covault, J. A. & Wooden, J. L. 2006. Does the Great Valley Group contain Jurassic strata? Re-evaluation of the age and early evolution of a classic foreland basin. *Geology* **34**, 21–4.

Tafti, R., Lang, J. R., Mortensen, J. K., Oliver, J. L. & Rebagliati, C. M. 2014. Geology and geochronology of the Xietongmen (Xiongcun) Cu–Au porphyry district, southern Tibet, China. *Economic Geology* **109**(7), 1967–2001.

https://doi.org/10.1017/S0016756818000122 Published online by Cambridge University Press

Tafti, R., Mortensen, J. K., Lang, J. R., Rebagliati, M. & Oliver, J. L. 2009. Jurassic U–Pb and Re–Os ages for the newly discovered Xietongmen Cu–Au porphyry district, Tibet, PRC: implications for metallogenic epochs in the southern Gangdese belt. *Economic Geology* **104**(1), 127–36.

Tang, H. F., Zhao, Z. Q., Han, R. S., Han, Y. J. & Su, Y. P. 2008. Primary Hf isotopic study on zircons from the A-type granites in Eastern Junggar of Xinjiang, northwest China. *Acta Mineralogica Sinica* **28**, 335–42 (in Chinese with English abstract).

Tang, J. X., Lang, X. H., Xie, F. W., Gao, Y. M., Li, Z. J., Huang, Y., Ding, F., Yang, H. H., Zhang, L., Wang, Q. & Zhou, Y. 2015. Geological characteristics and genesis of the Jurassic No. I porphyry Cu–Au deposit in the Xiongcun district, Gangdese porphyry copper belt, Tibet. *Ore Geology Reviews* **70**, 438–56.

Tang, J. X., Li, F. J., Li, Z. J., Zhang, L., Tang, X. Q., Deng, Q., Lang, X. H., Huang, Y., Yao, X. F. & Wang, Y. 2010. Period of time for the formation of main geologic bodies in Xiongcun copper-gold deposit, Xietongmen County, Tibet: evidence from Zircon U–Pb ages and Re–Os ages of molybdenite. *Mineral Deposits* **29**, 461–75 (in Chinese with English abstract).

Tang, J. X., Li, Z. J., Zhang, L., Huang, Y., Deng, Q. & Lang, X. H. 2007. Geological characteristic of the Xiongcun type porphyry-epithermal copper-gold deposit. *Acta Mineralogica Sinica* **S1**, 127–8 (in Chinese).

Taylor, S R & McLennan S, M. 1985. The continental crust: its composition and evolution, an examination of the geochemical record preserved in sedimentary rocks. *Journal of Geology* **94**(4), 632–33.

Tobia, F. H. & Aswad, K. J. 2014. Petrography and geochemistry of Jurassic sandstones, Western Desert, Iraq: implications on provenance and tectonic setting. *Arabian Journal of Geosciences* **8**(5), 2771–84.

Volkmer, J. E., Kapp, P., Guynn, J. H. & Lai, Q. 2007. Cretaceous–Tertiary structural evolution of the north central Lhasa terrane, Tibet. *Tectonics* **26**(6), TC6007.

Wang, C., Ding, L., Zhang, L. Y., Kapp, P., Pullen, A. & Yue, Y. H. 2016. Petrogenesis of Middle–Late triassic volcanic rocks from the gangdese belt, southern Lhasa terrane: implications for early subduction of Neo-tethyan oceanic lithosphere. *Lithos* **262**, 320–33.

Wang, R., Richards, J. P., Hou, Z. Q. & Yang, Z. M. 2014a. Extent of underthrusting of the Indian plate beneath Tibet controlled the distribution of Miocene porphyry Cu–Mo ± Au deposits. *Mineralium Deposita* **49**(2), 165–73.

Wang, R., Richards, J. P., Hou, Z., Yang, Z. & Dufrane, S. A. 2014b. Increased magmatic water content–the key to Oligo-Miocene porphyry Cu-Mo ± Au formation in the eastern Gangdese Belt, Tibet. *Economic Geology* **109**(5), 1315–39.

Wen, D. R., Liu, D., Chung, S. L., Chu, M. F., Ji, J., Zhang, Q., Song, B., Lee, T. Y., Yeh, M. W. & Lo, C. H. 2008. Zircon SHRIMP U–Pb ages of the Gangdese Batholith and implications for Neotethyan subduction in southern Tibet. *Chemical Geology* **252**(3), 191–201.

Wiedenbeck, M. A. P. C., Alle, P., Corfu, F., Griffin, W. L., Meier, M., Oberli, F., Von Quadt, A., Roddick, J. C. & Spiegel, W. 1995. Three natural zircon standards for U–Th–Pb, Lu–Hf, trace element and REE analyses. *Geostandards Newsletter* **19**(1), 1–23.

Winchester, J. A. & Max, M. D. 1989. Tectonic setting discrimination in clastic sequences: an example from late Proterozoic Erris Group, NW Ireland. *Precambrian Research* **45**, 191–201.

Yang, Z. M., Hou, Z. Q., Xia, D. X., Song, Y. C. & Li, Z. 2008. Relationship between Western Porphyry and mineralization in Qulong copper deposit of Tibet and enlightenment to further exploration. *Mineral Deposits* **27**, 28–36 (in Chinese with English abstract).

Yin, A. & Harrison, M. 2000. Geologic evolution of the Himalayan-Tibetan orogen. *Annual Review of Earth and Planetary Sciences* **28**, 211–80.

Yin, Q., Lang, X. H., Cui, Z. W., Yang, Z. Y., Xie, F. W. & Wang, X. H. 2017. Geology and geochemistry constraints on the genesis of the No.2 porphyry copper-gold deposit in the Xiongcun district, Gangdese porphyry copper belt, Tibet, China. *Applied Ecology and Environmental Research* **15**(3), 477–508.

Zhang, H. F., Xu, C. W., Guo, J. Q., Zong, K. Q., Cai, H. M. & Yuan, H. L. 2007. Indosinian orogenesis of the Gangdise terrane: evidences from zircon dating and petrogenesis of granitoids. *Earth Science-Journal of China University of Geosciences* **32**(2), 155–66 (in Chinese with English abstract).

Zhu, D. C., Pan, G. T., Chung, S. L., Liao, Z. L., Wang, L. Q. & Li, G. M. 2008. SHRIMP zircon age and geochemical constraints on the origin of Lower Jurassic volcanic rocks from the Yeba Formation, southern Gangdese, south Tibet. *International Geology Review* **50**, 442–71.

Zhu, D. C., Zhao, Z. D., Niu, Y. L., Dilek, Y., Wang, L. Q. & Mo, X. X. 2011a. Lhasa terrane in southern Tibet came from Australia. *Geology* **39**, 727–30.

Zhu, D. C., Zhao, Z. D., Niu, Y. L., Mo, X. X., Chung, S. L., Hou, Z. Q., Wang, L. Q. & Wu, F. Y. 2011b. The Lhasa Terrane: Record of a microcontinent and its histories of drift and growth. *Earth and Planetary Science Letters* **301**, 241–55.

Zhu, D. C., Zhao, Z. D., Pan, G. T., Lee, Y. H., Kang, Z. Q., Liao, Z. L., Wang, L. Q., Li, G. M., Dong, G. C. & Liu, B. 2009. Early cretaceous subduction-related adakite-like rocks of the Gangdese Belt, southern Tibet: products of slab melting and subsequent melt-peridotite interaction? *Journal of Asian Earth Sciences* **34**, 298–309.

https://doi.org/10.1017/S0016756818000122 Published online by Cambridge University Press